frontiers | Frontiers in Earth Science

ORIGINAL RESEARCH
published: 01 April 2022
doi: 10.3389/feart.2022.761902

Mantle and Crustal Xenoliths in a Tephriphonolite From La Palma (Canary Islands): Implications for Phonolite Formation at Oceanic Island Volcanoes

Andreas Klügel[1]*, *Elmar Albers*[1] and *Thor H. Hansteen*[2]

[1]Fachbereich Geowissenschaften, Universität Bremen, Bremen, Germany, [2]GEOMAR Helmholtz-Zentrum für Ozeanforschung Kiel, Kiel, Germany

The occurrence of mantle-derived peridotite xenoliths in phonolitic melts is a rare phenomenon, and is commonly ascribed to a mantle origin of the phonolite. The alternative possibility, that xenoliths are transported into evolving phonolite melts by mafic magmas, has received little attention. A unique tephriphonolite lava with phonolitic groundmass composition, from the active Cumbre Vieja volcano of La Palma (Canary Islands), allows to test these models. The lava contains abundant inclusions that represent the island's major xenolith types: kaersutite-dominated cumulates, gabbros from the lower oceanic crust, and peridotites from the mantle. Our petrological investigations indicate that the tephriphonolite magma contained 3–4 wt% H_2O and was stored in the lower crust at around 250–350 MPa and 900–950°C, at oxidized conditions (ΔNNO of 2–3). The peridotite xenoliths are mantled by complex polyphase selvages, with adjacent up to 1.6 mm wide zonations where olivine compositions change from Fo_{78-86} at the selvage contact to Fo_{89-91} inside the xenoliths. We carried out diffusion modelling for Fe-Mg exchange and found that the peridotites had contact with intermediate to evolved alkaline melts over decades to centuries. This timescale is comparable to that inferred for basanite-hosted peridotite xenoliths from Cumbre Vieja. The following model is proposed: differentiation of evolved melts occurs in a magma accumulation zone in the lowermost oceanic crust beneath La Palma. The evolving melts receive periodic recharge by mantle-derived mafic magmas at intervals on the order of decades to a few centuries, comparable to historic eruption recurrences (80 years on average). Some of these recharge pulses carry mantle peridotite fragments that become deposited in the accumulation zone. Thus, these xenoliths do not reflect formation of the evolved melts in the mantle. Final ascent of the tephriphonolite was triggered by magma recharge some weeks before its eruption, resulting in entrainment and thorough mingling of a mixed xenolith population (cumulates, oceanic crust gabbros, peridotites). We infer that formation of phonolites in the lower crust beneath oceanic island volcanoes, and subsequent eruption, requires a balance between rates and volumes of magma recharge pulses and of eruptive events.

Keywords: magma storage, phonolite, differentiation, thermobarometry, intraplate volcanism

OPEN ACCESS

Edited by:
Michel Pichavant, CNRS Orléans, France

Reviewed by:
Abigail Barker, Uppsala University, Sweden
Joan Andújar, UMR7327 Institut des sciences de la Terre d'Orléans (ISTO), France

***Correspondence:**
Andreas Klügel
akluegel@uni-bremen.de

Specialty section:
This article was submitted to Volcanology, a section of the journal Frontiers in Earth Science

Received: *20 August 2021*
Accepted: *18 February 2022*
Published: *01 April 2022*

Citation:
Klügel A, Albers E and Hansteen TH (2022) Mantle and Crustal Xenoliths in a Tephriphonolite From La Palma (Canary Islands): Implications for Phonolite Formation at Oceanic Island Volcanoes. Front. Earth Sci. 10:761902. doi: 10.3389/feart.2022.761902

INTRODUCTION

Phonolites, the differentiated residual end-members of alkaline, SiO_2-undersaturated melts, are typical products of intraplate magmatism. They are widespread on Earth but are volumetrically subordinate to corresponding alkaline basalts in most places, with the Miocene flood phonolites of the Kenya Rift as a notable exception (Hay and Wendlandt, 1995). Phonolite domes, cryptodomes, and lava flows form prominent deposits and outcrops on many volcanic islands, for example La Gomera, La Palma and Tenerife (Canary Islands), Brava and Santo Antão (Cabo Verde Islands), São Tomé, Trindade, Tristan da Cunha, and Kerguelen archipelago (e.g. Mitchell-Thomé, 1970; Schmincke, 1976; Weaver, 1990; Weis et al., 1993). Pyroclastic deposits from strongly explosive phonolite eruptions are major features e.g. on Tenerife, Brava and Santo Antão islands (e.g., Martí et al., 1994; Edgar et al., 2007; Mortensen et al., 2009; Madeira et al., 2010). Phonolites can occur during the early seamount stage of a volcano, such as Cadamosto at Cabo Verde archipelago (Barker et al., 2012) and near Tahiti and the Pitcairn islands (Devey et al., 2003), as well as during later stages or episodes as on Tenerife and Brava (e.g., Ablay et al., 1998; Madeira et al., 2010).

Phonolites are commonly derived from alkaline basaltic melts through extensive, often polybaric fractional crystallization, consistent with observed phenocryst phases and the liquid lines of descent (LLD) for basalt-phonolite series (e.g., Price and Chappell, 1975; Wörner and Schmincke, 1984; LeRoex et al., 1990; Weaver, 1990; Ablay et al., 1998; Johansen et al., 2005; Melluso et al., 2007; Turner et al., 2015; Berthod et al., 2021). U-series isotope studies suggest times of differentiation from basanite to phonolite ranging from ~100 to 1,600 years for small systems (Johansen et al., 2005; Reagan et al., 2008) to 100–230 ka for larger systems (Bourdon et al., 1994; Hawkesworth et al., 2000). Pre-eruptive phonolite evolution at relatively shallow levels (<300 MPa) is indicated by volatile concentrations of trapped melts and mineral barometry (Ablay et al., 1998; Marziano et al., 2007; Schmidt and Behrens, 2008), feldspar fractionation (Price and Chappell, 1975; Kelly et al., 2008), and experimental work (e.g., Berndt et al., 2001; Freise et al., 2003; Harms et al., 2004; Andújar et al., 2008, 2010, 2013; Moussallam et al., 2013). Phonolites may also form at high pressures without feldspar fractionation (1–2 GPa; Kunzmann, 1996; Irving and Price, 1981; Irving and Green, 2008; Grant et al., 2013). In rare cases, phonolites or tephriphonolites carry peridotite xenoliths from the mantle, the only occurrences reported thus far being Phonolite Hill (Australia), Dunedin Volcanic Complex (New Zealand), Bokkos (Nigeria), Heldburg (Germany), Harrat Kishb (Saudi Arabia), and Mayotte Island (Comoros archipelago) (Wright, 1966; Irving and Price, 1981; Irving and Green, 2008; Grant et al., 2013; Berthod et al., 2021).

The occurrence of mantle xenoliths in a phonolite likely reflects a mantle origin of the magma, but unless demonstrated by e.g. barometric data (Grant et al., 2013; Berthod et al., 2021) such an interpretation may be misleading. Recharge events during magma differentiation at shallower levels (e.g., Rout and Wörner, 2020) may also bring deep-seated fragments into an evolving melt. Here we present petrological data from a unique tephriphonolite body on La Palma (Canary Islands), which carries abundant mantle and crustal xenoliths in a phonolitic groundmass. We demonstrate that the magma was stored in the crust and received peridotite fragments by mafic recharge, constrain the timing of recharge events, and discuss the implications for magma storage and eruption.

GEOLOGICAL SETTING

The Canary Archipelago is a chain of seven volcanic islands located off the northwestern African continental shelf (**Figure 1**). They form the western branch of an intraplate hotspot chain with seamount and island ages decreasing from east to west (Geldmacher et al., 2005). All islands are underlain by Jurassic oceanic crust as is indicated by mid-ocean ridge basalt (MORB) gabbro xenoliths occurring on Lanzarote, Gran Canaria, and La Palma (Hoernle, 1998; Schmincke et al., 1998). The age of the crust is 175 Ma between Lanzarote and the African coast (paleomagnetic anomaly S1), and 155 Ma between La Palma and El Hierro, the westernmost and youngest islands (M25; Klitgord and Schouten, 1986).

The geology of La Palma is extensively summarized in Carracedo et al. (2001). Briefly, the island consists of three main units: *1*) the basal complex (4.0–2.9 Ma) which comprises a Pliocene seamount sequence and a plutonic complex; *2*) the older volcanic series (1.7–0.41 Ma) which includes the Taburiente shield volcano and the Bejenado edifice; and *3*) the Cumbre Vieja series (>125 ka to present) confined to the southern half of the island (**Figure 1A**). La Palma is currently in the latter part of its shield-building stage. With seven eruptions recorded since the 15th century, the north-south trending Cumbre Vieja ridge is an active volcanic rift zone along which most scoria cones, eruptive fissures and faults are concentrated (Middlemost, 1972; Hernandéz-Pacheco and Valls, 1982; Carracedo, 1994).

Cumbre Vieja rocks are Si-undersaturated and alkaline, with most compositions following a basanite-phonolite lineage (summarized in Carracedo et al., 2001). The major phenocryst phases are titaniferous clinopyroxene ± olivine + Ti-magnetite ± kaersutitic amphibole in the mafic Cumbre Vieja rocks, and clinopyroxene + kaersutite + magnetite + plagioclase ± haüyne ± titanite ± apatite in the evolved rocks. Xenoliths are commonly found in late erupted basanites, including ultramafic cumulates (the most common type), mafic cumulates, MORB-type gabbros from the Jurassic ocean crust, mantle peridotites, and various types of felsic fragments (Klügel et al., 1999). Whereas phonolites are virtually absent in the older volcanic series and rare at Bejenado volcano, they commonly occur at

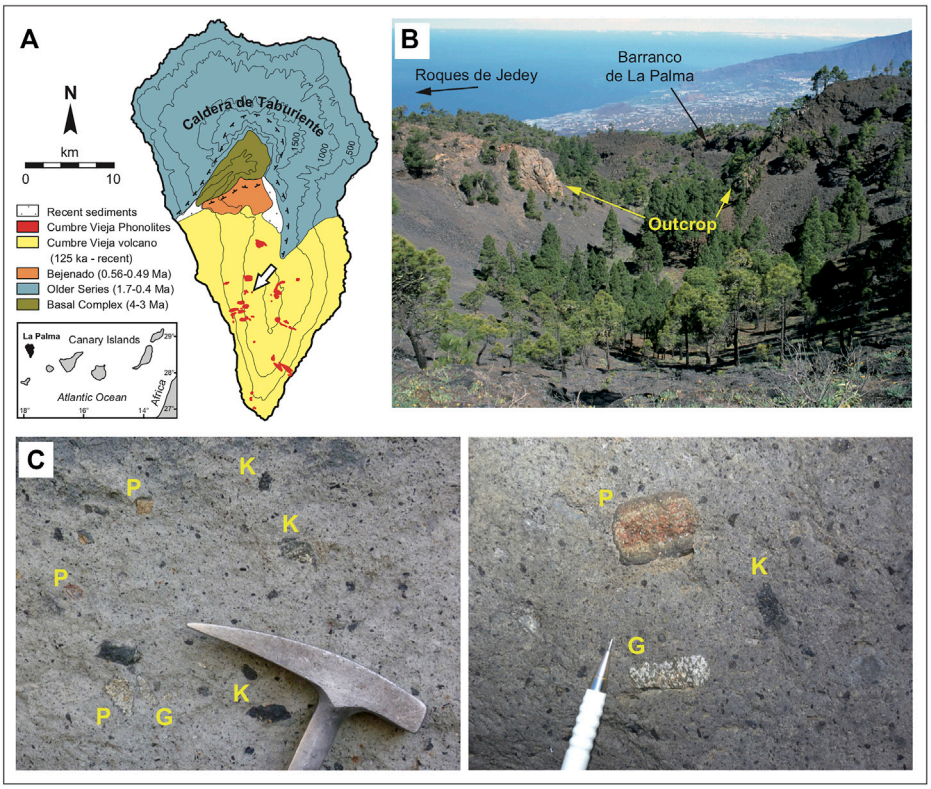

FIGURE 1 | (A) Simplified geological map of La Palma with arrow showing the locality of the tephriphonolite outcrops. **(B)** Photograph towards the northwest, showing the breached 1585 eruption crater with the tephriphonolite outcrops (arrows). **(C)** Outcrop photographs of the tephriphonolite with kaersutitite (K), gabbro (G), and peridotite (P) xenoliths. Note the selvage around the peridotites.

Cumbre Vieja as domes, spines and lava flows (Hernandéz-Pacheco and De la Nuez, 1983) (**Figure 1**). During the catastrophic 1585 eruption, a pre-existing phonolitic dome was uplifted and a juvenile phonolitic cryptodome was emplaced (Day et al., 1999).

The peridotite-bearing tephriphonolite investigated here crops out at the breached wall of the north-easternmost crater of the 1585 Tahuya eruption, 1 km east of the prominent Roques de Jedey phonolite spines and 200 m south of Barranco de La Palma, at 1,200–1,230 m above sea level (**Figure 1B**). The overall joint patterns, flow markers, and steeply west-dipping banks of brecciated rock visible at the northern outcrop cliff suggest that the tephriphonolite was extruded at this site along a N-S trending fissure. This is consistent with the presence of decimeter-sized, partly rounded blocks up to 1 km downslope. Angular tephriphonolite lithic fragments are widespread around the outcrop; apparently they were produced during the 1585 eruption when violent explosions excavated the north-easternmost crater and the tephriphonolite plug (Romero Ruiz, 1991; Day et al., 1999). The tephriphonolite hence pre-dates the 1585 eruption, but its exact age is unknown. Overall, this tephriphonolite is easily recognized in the field due to the abundance of ultramafic cumulate, gabbro, and peridotite xenoliths up to 5 cm in size (**Figure 1C**). A list of the samples from this study and their localities is given in **Supplementary Table S1**.

METHODS

Whole-Rock Analyses

Three selected tephriphonolite samples were crushed and sieved, fragments containing xenoliths were removed, and the remaining separates were powderized using an agate mill. Whole-rock analyses of the tephriphonolite were carried out by X-ray fluorescence spectrometry (XRF) on fused glass beads using a Philips X'Unique PW1480 at GEOMAR (Kiel) calibrated with international standards. H_2O and CO_2 were analysed with a Rosemount CSA 5003 infrared photometer. The samples were also analyzed for trace elements by inductively coupled plasma-mass spectrometry (ICP-MS) at the Department of Earth Science, Memorial University of Newfoundland, following the procedure described in Jenner et al. (1990). Whole-rock analyses of four other tephriphonolites and phonolites were carried out on fused lithium-tetraborate glass beads using a Pananalytical Magix PRO XRF at the Mineralogisch-Petrographisches Institut, Universität Hamburg, Germany. Loss on ignition (LOI) was determined gravimetrically after fusion of a sample aliquot at 1,050°C (Lechler and Desilets, 1987). Analyses of secondary standards

are given in **Supplementary Table S2**. Accuracy of XRF standard data is better than 2 and 10% for concentrations of >1 wt% and >0.1 wt%, respectively. Accuracy of ICP-MS data is better than 5% for most trace elements and better than 10% overall except for Pb (16%).

Groundmass Analyses

The major element composition of groundmass was determined on thin sections by laser ablation ICP-MS at the Faculty of Geosciences, University of Bremen, using a NewWave UP193ss laser coupled to a Thermo Element2. Helium (~0.8 L/min) was used as sample gas and Argon (~0.8 L/min) was subsequently added as make-up gas; plasma power was 1200 W. A laser beam of 100 µm diameter and 5 Hz pulse rate was moved over groundmass at 5–6 µm/s for 60–180 s to give a single analysis; four to eight such analyses were averaged. The isotopes ^{23}Na, ^{24}Mg, ^{27}Al, ^{28}Si, ^{31}P, ^{39}K, ^{44}Ca, ^{48}Ti, ^{55}Mn and ^{56}Fe were analyzed at high resolution with a 150% mass window and a total dwell time of 0.15 s per isotope. Blanks were measured during 25 s prior to ablation. The data were quantified using the Cetac GeoPro™ software with USGS glass BCR-2G as external calibration standard (Jochum et al., 2005) and Ca as internal standard element. The Ca concentration was initially set to an arbitrary value, and calculated concentrations were subsequently normalized to a volatile-free sum of 100 wt% oxides with total Fe as FeO. Analytical precision and accuracy were monitored by regular analyses of USGS basalt glass BHVO-2G (Jochum et al., 2005) along with the samples; both were <2% for most elements and <8% throughout (**Supplementary Table S3**).

Electron Microprobe Analyses

Electron microprobe (EMP) analyses of minerals were carried out on Jeol JXA-8900RL (Geosciences Institute, Universities of Mainz and Kiel), Cameca SX-50 (GEOMAR, Kiel), and Cameca SX-100 instruments (Faculty of Geosciences, Bremen). Analytical conditions included peak counting times of 15–20 s, an acceleration voltage of 15 kV, beam diameter between 1 and 5 µm, and beam currents of 30–50 nA for olivine and 10–15 nA for other minerals. The instruments were calibrated with reference standards mainly from the Smithsonian Institution (Jarosewich et al., 1980). The built-in PRZ (Jeol) and PAP (Cameca) correction methods were applied for data reduction. Analytical precision and accuracy were controlled by regular analyses of secondary standards (**Supplementary Table S4**). Qualitative wavelength-dispersive spectrometer (WDS) analyses of Si, Mg, Fe and Ca along olivine traverses were carried out with 50 nA beam current and dwell times of 1 s per point.

Microthermometry

Fluid inclusions used for barometry were examined in 100 µm thick doubly polished sections. Microthermometric analyses were carried out on small chips from these sections using a Linkam THM 600 heating-cooling stage at GEOMAR, Kiel. The stage was calibrated with SYNFLINC™ fluid inclusion standards at −56.6°C, 0.0°C, and 374.1°C. Accuracy of CO_2 triple-point measurements and reproducibility of melting and homogenization temperatures were within ±0.2°C. Densities of CO_2-dominated inclusions were calculated from measured homogenization temperatures using the auxiliary Eqs 3.14 and 3.15 of Span and Wagner (1996). Isochores were computed with the Sterner and Pitzer (1994) equation of state for the CO_2-H_2O system, following Hansteen and Klügel (2008).

RESULTS

Petrography and Mineral and Melt Compositions

Modal mineral proportions in lavas and xenoliths were determined on thin sections by visual estimates. Whole-rock and groundmass compositions of tephriphonolite and phonolite samples are presented in **Supplementary Table S5**; the compositions of all minerals analyzed are provided in **Supplementary Tables S6–S10**. Scanned images of entire thin sections are presented in **Supplementary Figure S1**.

Host Tephriphonolite

The xenolith-rich tephriphonolite contains up to 10 vol% of irregularly shaped vesicles that were deformed and disrupted by shearing of the viscous magma. The groundmass consists of anorthoclase laths with subordinate Ti-magnetite, clinopyroxene, apatite, minor haüyne, rare zircon (as a late-stage phase occurring close to vesicles), ±glass. The macrocryst phases (>0.1 mm) are kaersutitic amphibole (10–20 vol%, up to 4 mm in size), greenish clinopyroxene (<5%, <1 mm), plagioclase (<5%, <1 mm), haüyne (<5%, <0.5 mm), apatite (<1%, <0.5 mm), and Ti-magnetite (1–2%, <0.5 mm) (**Figures 2A,D** and **Supplementary Figure S1**). Titanite is not present, in contrast to the more evolved Cumbre Vieja phonolites. Most macrocrysts are euhedral to subhedral, but there are also irregularly-shaped crystal fragments and small amphibole/clinopyroxene-rich polycrystalline aggregates, interpreted as xenocrysts and xenolith fragments. Kaersutites commonly display 20–80 µm thick fine-grained opaque reaction rims (opacite), indicating reaction with the host melt (Rutherford and Hill, 1993; De Angelis et al., 2015; France, 2020). Likewise, most haüynes are corroded with 10–60 µm thick opaque reaction rims towards the host melt. Apatite occurs as phenocrysts with locally corroded rims, and as ubiquitous inclusions in kaersutite and clinopyroxene. Locally the feldspar laths and macrocrysts define a flow texture.

Plagioclase has a compositional range $Ab_{48\text{-}60}An_{30\text{-}46}Or_{4\text{-}10}$, showing a gradual transition in composition and size toward the less anorthitic groundmass anorthoclase. Kaersutite has a range in Mg# from 52 to 71 (Mg# = molar Mg/(Mg+Fe_{tot})*100), SiO_2 from 38.6 to 40.9 wt%, and TiO_2 from 4.2 to 5.6 wt% (**Figure 3A**). Many crystals display normal progressive zoning with decreasing Mg# towards the rim (Mg# 66–71 to 52–58; **Figure 3C**); crystals that are more complexly zoned and/or display an optically distinct core are less common. The compositions indicate moderate correlation of Mg# with Na, Al, Ti, and Si with significant scatter, interpreted to reflect a broad fractionation trend (**Figure 3A**). Clinopyroxene is ferrian aluminian diopside

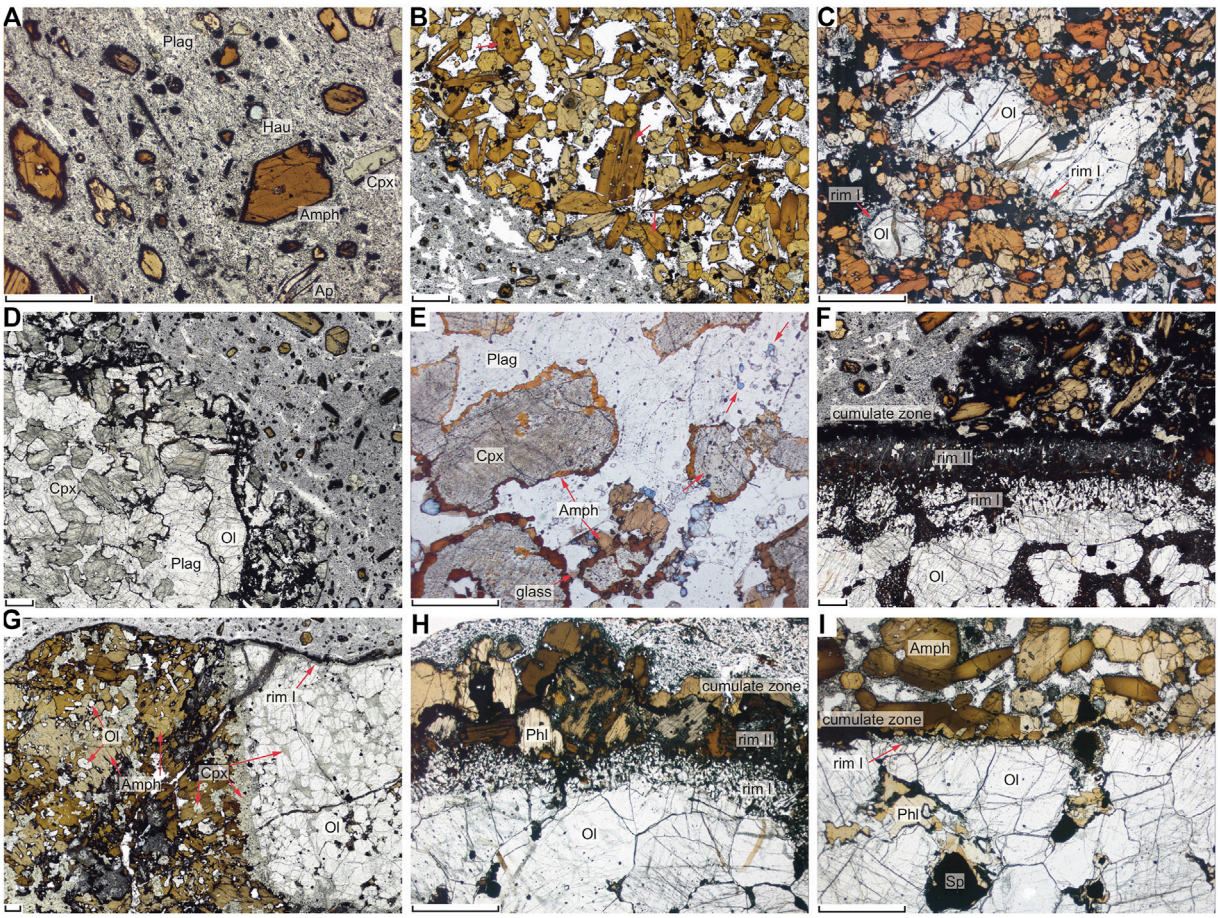

FIGURE 2 | Microphotographs from selected samples taken at plane polarized light; scale bars are 1 mm. Abbreviations: Cpx, clinopyroxene; Amph, amphibole; Plag, plagioclase; Ol, olivine; Phl, phlogopite; Sp, spinel; Ap, apatite; Hau, haüyne. **(A)** Sample KLA1718: tephriphonolite with kaersutite, clinopyroxene, plagioclase, haüyne, and apatite macrocrysts. **(B)** Sample KLA1705: kaersutite-dominated cumulate xenolith with open texture; host tephriphonolite to the lower left. Arrows indicate examples of strongly zoned crystals. **(C)** Sample KLA1709: olivine and small peridotite fragment with reaction rim of Cpx+Mt within kaersutite-dominated cumulate xenolith. **(D)** Sample KLA1701: olivine gabbro xenolith with incipient melting at grain boundaries; degree of melting increases towards the host tephriphonolite contact (upper right). **(E)** Sample KLA1708: strongly metasomatized gabbro xenolith with blue haüyne and brown amphibole around clinopyroxene. Note the presence of glass, euhedral Amph, euhedral haüyne within newly crystallized Plag, and recrystallized Cpx along a NE-SW trending vein (arrows). **(F)** Sample KLA1704: spinel wehrlite xenolith (bottom) with cumulus texture and Cpx that is in large parts replaced by opaque Phl-rich aggregates. The xenolith has a prominent selvage towards the host tephriphonolite (top) consisting of Cpx-Mt-dominated rim I, Phl-dominated rim II, and Amph-rich cumulate zone. **(G)** Sample KLA1735: composite xenolith with veined wehrlite (right) and cumulate dominated by brown Amph oikocrysts, subhedral Ol, and Cpx (left). The wehrlite has a thick Cpx-Mt selvage towards the cumulate, and a thin selvage towards the host tephriphonolite (top). **(H)** Sample KLA1731: dunite xenolith (bottom) with selvage consisting of Cpx-Mt-dominated rim I, Phl-dominated rim II, and Amph-rich cumulate zone. **(I)** Sample KLA1721: peridotite xenolith (bottom) with metasomatic Phl and two-part selvage, consisting of a narrow Cpx+Mt dominated reaction rim I and an Amph-dominated cumulate zone; rim II is absent in this sample.

with considerable variation in composition (Mg# 55–77, SiO_2 43–51 wt%, TiO_2 1.0–3.4 wt%, Na_2O 0.8–2.5 wt%, Al_2O_3 1.7–7.8 wt%; **Figure 3B**). Clinopyroxene macrocrysts can be variably zoned and display complex compositional profiles; reverse and step zoning are not uncommon (**Figure 3D**). The interiors span a larger Mg# range than the rims, with a tendency to higher Si and Na, and lower Al and Ti, at a given Mg#. The interiors and rims broadly define two distinct compositional trends (**Figure 3B**): trend 1) is interpreted to reflect chemical variations during magma evolution and broadly resembles the variations of kaersutite macrocrysts (**Figure 3A**), whilst trend 2) is opposite in some diagrams. Trend 2) can be explained by sector zoning, which produces hourglass {−111} basal sectors that are higher in Mg# and SiO_2, and lower in Al_2O_3 and TiO_2, than {hk0} prism sectors (Ubide et al., 2019). This zoning can be formally expressed by coupled cation exchange between {−111} and {hk0} sectors, resulting in positive correlation of Mg# with Si and negative correlation with Al and Ti (Welsch et al., 2016; Ubide et al., 2019), as observed in **Figure 3B**. Sector zoning can be the dominating trend in clinopyroxene assemblages, making any specific fractionation trend almost unrecognizeable (cf. Ubide et al., 2019). Compared to the rims of macrocrysts in mafic Cumbre Vieja lavas, tephriphonolite clinopyroxenes are more Na-rich and define distinct compositional fields (**Figure 3B**). Overall the large Mg# ranges of the inner regions of clinopyroxene and kaersutite macrocrysts, as well as the reverse and complex zonings observed,

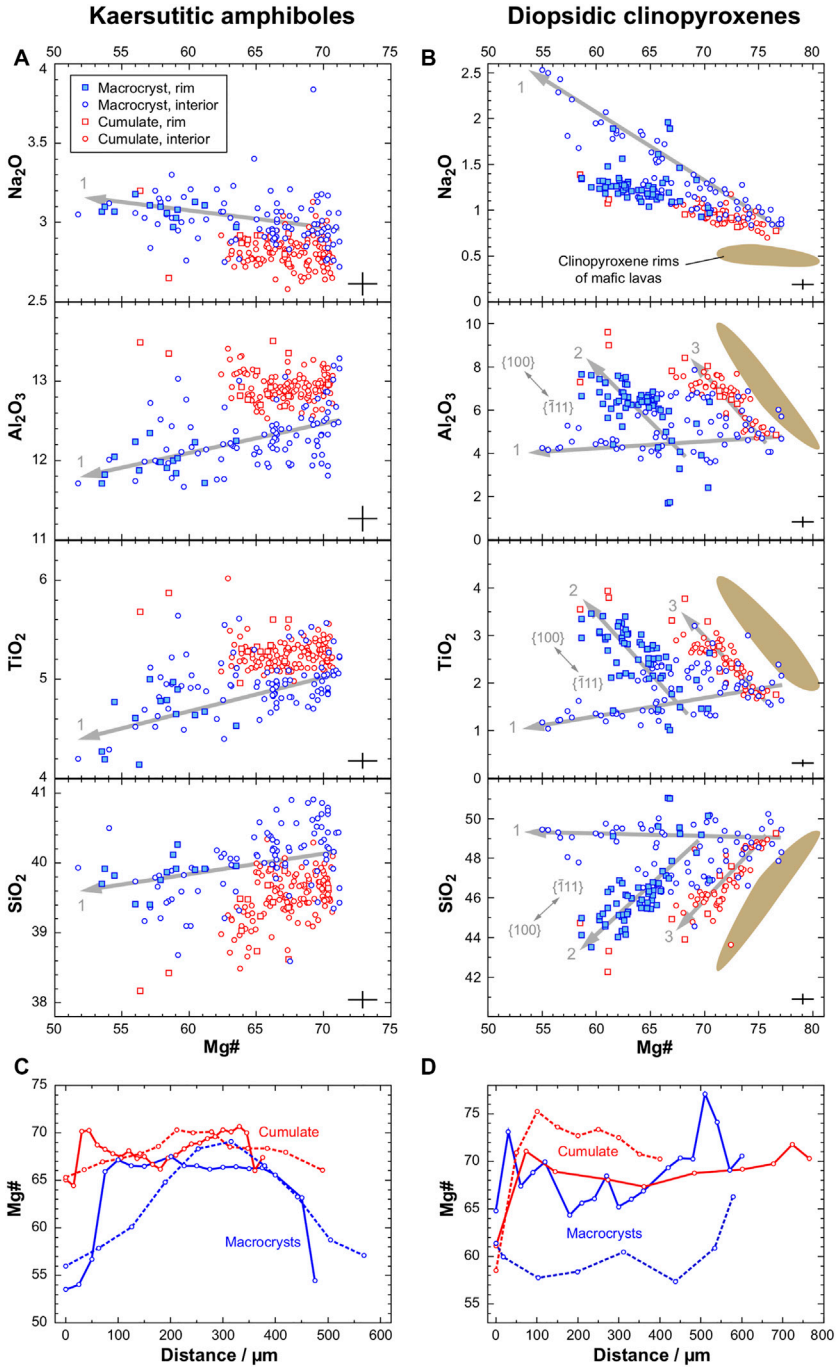

FIGURE 3 | Chemical compositions of **(A)** kaersutite and **(B)** diopside macrocrysts in the host tephriphonolite (blue symbols) and in cumulate xenoliths (red symbols) plotted in bivariate diagrams versus Mg#. Analyses at the outermost crystal rims are indicated by squares, those in the inner regions by circles. Brown fields outline average compositions of rims of clinopyroxene macrocrysts hosted by mafic lavas (basanites and tephrites; Klügel et al., 2000, 2005). Error bars indicate analytical uncertainty (±1 standard deviation) as based on analyses of secondary standards. Cumulate crystals show limited compositional overlap with macrocrysts and a smaller compositional range. Clinopyroxene compositions define three major trends indicated by thick arrows: trend 1) is interpreted to reflect progressive crystal fractionation, whereas trends 2) and 3) show opposite behavior for some elements. These trends are consistent with sector zoning, in which hourglass {−111} basal sectors are higher in Mg# and SiO_2, and lower in Al_2O_3 and TiO_2, than {100} prism sectors (cf. Ubide et al., 2019). The fractionation trend 1) is also broadly recognized in kaersutite macrocrysts. **(C,D)** Compositional profiles showing Mg# of selected kaersutite and diopside crystals, respectively.

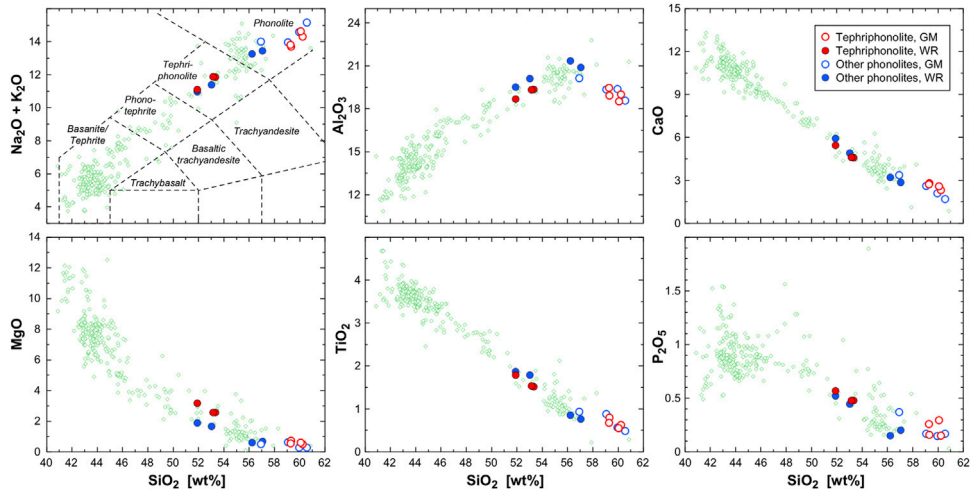

FIGURE 4 | Harker diagrams for samples from the investigated tephriphonolite (red filled circles) and its groundmass (red-white circles), from four other tephriphonolites to phonolites from Cumbre Vieja (blue filled circles) and their groundmass (blue-white circles), and from other historic and prehistoric Cumbre Vieja rocks (green diamonds; data from Hernandéz-Pacheco and Valls (1982), Hernandéz-Pacheco and de la Nuez (1983), Elliott (1991), Klügel et al. (2000); Klügel et al. (2017), Carracedo et al. (2001), Johansen et al. (2005), Day et al. (2010), Turner et al. (2015)). Data are normalized to 100% volatile-free. WR, whole-rock; GM, groundmass. The trends in the diagrams are consistent with fractionation of the phenocryst phases observed.

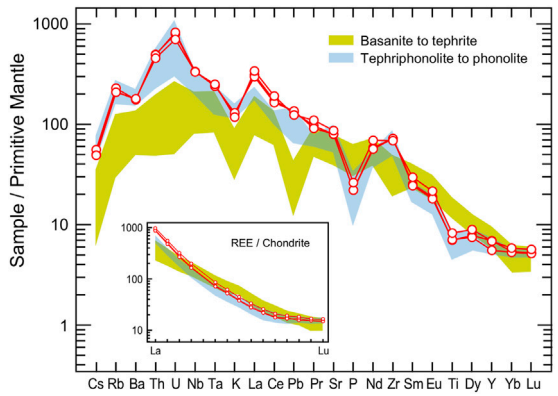

FIGURE 5 | Incompatible-element diagram for three tephriphonolite samples of this study, normalized to primitive mantle. Range for basanites and tephrites (green), and tephriphonolites and phonolites (blue), from Cumbre Vieja are indicated for comparison; data sources as in **Figure 4**. Inset shows the pronounced concave-upward shape of the samples in a chondrite-normalized REE diagram. Normalization values are from Sun and McDonough (1989).

indicate a considerable portion of antecrysts and xenocrysts in the tephriphonolite.

The whole rock contains around 52–53 wt% SiO_2 and falls within the basanite-phonolite lineage of Cumbre Vieja. This lineage is controlled by crystal fractionation and subordinate magma mixing, as is demonstrated by mass-balance calculations (Johansen et al., 2005; Turner et al., 2015). The groundmass of the tephriphonolite has phonolitic composition with around 59–60 wt% SiO_2 (**Figure 4**). The decrease of CaO, TiO_2 and MgO with increasing SiO_2 is consistent with removal of clinopyroxene and kaersutitic amphibole, the main macrocryst phases in tephrites to phonolites from Cumbre Vieja. The depletion in Al_2O_3 of phonolitic groundmass but not in the whole-rock trend (**Figure 4**) suggests that phonolites underwent only little feldspar fractionation. Variations between samples in groundmass composition and macrocryst content indicate some heterogeneities of the tephriphonolite body. Incompatible trace element patterns of the tephriphonolite broadly follow those of other evolved rocks from the Cumbre Vieja (**Figure 5**). Negative Ti anomalies, low Nb/U and Ba/Th ratios, and concave-upward spectra of the rare earth elements (REE) are consistent with extensive kaersutite fractionation, in accordance with the petrographic observations. Likewise, removal of apatite can explain the negative P anomalies observed, as well as decreasing P_2O_5 with increasing SiO_2 (**Figure 4**). In contrast to basanites and tephrites, the tephriphonolite as well as other evolved rocks from the Cumbre Vieja show low Ce/Pb ratios (11–15) and no negative Pb anomalies.

Kaersutitite Xenoliths

These ultramafic xenoliths consist of kaersutitic amphibole as the dominant phase (50–90 vol%, up to 4 mm in size), greenish aluminian diopside (2–30%, <3 mm), apatite (2–5%, <1 mm), anorthoclase feldspar (2–5%, <0.5 mm), Ti-magnetite (1–5%, <0.5 mm), and accessory zircon (**Figure 2B**). Some samples contain olivine xenocrysts or aggregates with symplectitic reaction rims of clinopyroxene and magnetite (**Figure 2C**). The xenoliths show an open cumulus texture with dominantly euhedral to subhedral crystals and up to 20 vol% of voids in the interstices (**Figure 2B**). Much of the interstitial space is filled with anorthoclase and minor zircon representing the last crystallizing phases; we note that zircon is a very rare phase in igneous rocks

from Cumbre Vieja. In thin section, kaersutite and diopside crystals commonly show patchy or concentric zoning, in some cases an optically distinct core, and in many cases a distinct outermost rim (**Figure 2B**). Some kaersutites exhibit opacite rims at the contact to the interstices and to the host tephriphonolite, but not at the contact to other crystals. Apatite occurs as a cumulus phase with marginally corroded crystals similar to those in the host tephriphonolite, and also as ubiquitous inclusions in kaersutite and clinopyroxene. Locally, incipient disintegration at the xenolith surface results in a transition from cumulus texture to macrocrysts in host magma (**Figure 2B**). In contrast to the xenoliths studied here, basanite-hosted kaersutite- and clinopyroxene-dominated cumulate xenoliths that are ubiquitous on Cumbre Vieja have a more primitive character, as is expressed by the presence of olivine and the lack of apatite and anorthoclase feldspar (Muñoz et al., 1974; Klügel et al., 1999; Barker et al., 2015).

Chemical compositions of kaersutite and diopside in the xenoliths partly overlap with those of tephriphonolite macrocrysts and show less variability. Compared to the macrocrysts, xenolith kaersutites tend to be lower in Si and Na, higher in Ti and Al, and more restricted in Mg# (**Figure 3A**). Xenolith diopsides define a unique compositional trend 3) that broadly resembles trend 2) for tephriphonolite macrocrysts, but is shifted to higher Mg# and lower Na (**Figure 3B**). As discussed above, this trend likely reflects sector zonations of the crystals. Diopside rims have a tendency to lower Mg# and Si, and higher Al and Ti than the inner regions, but overall there is strong overlap between interior and outermost rim compositions (**Figures 3A,B**). Cumulus crystals can be variably zoned, including normal zoning with decreasing Mg# from core to rim, or more complex zoning with an increase and subsequent decrease in Mg# from core to rim (**Figures 3C,D**). The compositions of xenolith feldspar ($Ab_{45-65}An_{4-44}Or_{7-43}$) overlap those of the groundmass anorthoclase but extend to less anorthitic and more potassic compositions.

Gabbro Xenoliths

The gabbro xenoliths consist of plagioclase (30–50 vol%), diopsidic clinopyroxene (40–60 vol%), olivine (0–20 vol%), occasional orthopyroxene, and accessory Ti-magnetite (**Figure 2D**). Clinopyroxene commonly shows exsolution lamellae of orthopyroxene. Clinopyroxene compositions differ markedly from those of La Palma lavas (**Figure 3B**) by higher Mg# (80.8–83.6) and SiO_2 (51.7–53.5 wt%), and lower TiO_2 (0.2–0.5 wt%), Al_2O_3 (1.0–2.9 wt%), and Na_2O (0.3–1.2 wt%). These compositions partly overlap with those from MORB-type gabbros of the oceanic crust (Schmincke et al., 1998). Most gabbros are <3 cm in size, medium-grained (0.5–3 mm), and isotropic or mildly foliated. Local intracrystalline deformation is expressed as deformation twins in plagioclase and undulose extinction in plagioclase and olivine. Some gabbros record pervasive overprinting and/or modal metasomatism by alkaline La Palma melts and related fluids (cf. Neumann et al., 2000). This includes ubiquitous fluid and melt inclusions that occur randomly distributed or as trails within and across gabbro crystals (**Figure 2E**). Incipient partial melting of the xenoliths is indicated by sieve textures in clinopyroxene, and by very fine-grained dark zones of recrystallized material along plagioclase-clinopyroxene and plagioclase-olivine contacts. The width and proportion of these dark zones commonly increase towards the host magma contact (**Figure 2D**); locally they form an interconnected network. In some gabbros reaction with alkaline melts resulted in reaction rims of brown Ti-rich amphibole around clinopyroxene, and in the introduction of haüyne within or next to plagioclase (**Figure 2E**). The occurrence of euhedral haüyne crystals within gabbro plagioclase is remarkable, as it indicates a considerable degree of melting with renewed crystallization of plagioclase, and hence a high temperature of metasomatism. The reaction zones of the gabbros toward the host tephriphonolite can grade into cumulate-like zones with open textures and increasing proportion of host magma minerals (**Figure 2E**), marking a precursory stage of xenolith disintegration and assimilation.

Peridotite Xenoliths

Peridotitic xenoliths in the tephriphonolite cover a wide textural and compositional range (**Figures 2F–I**). The xenoliths studied here are spinel- and phlogopite-bearing wehrlite, dunite, and lherzolite with 60–97 percent of modal olivine; this classification uses the original proportions of clinopyroxene before its replacement by other phases. All xenoliths are hydrous, containing up to 25 vol% of phlogopite and in some cases pargasitic to kaersutitic amphibole. Wehrlites commonly show a cumulate-like framework of anhedral to subhedral olivine up to 5 mm in size (samples KLA1704, −1715, −1718, −1735; **Figures 2F,G**). Interstitial and intergranular space makes up to 36 vol%; it is dominated by clinopyroxene, spinel, and complex phlogopite-rich aggregates that appear opaque in thin section where fine-grained phlogopite ± Fe-Ti oxides prevail (**Figure 2F**). In many places clinopyroxene is partly to completely replaced by phlogopite-rich assemblages, as recognized by optical continuity of clinopyroxene remnants. Other samples (KLA1721, -1731) have an olivine grain-supported texture with little interstitial space (**Figures 2H,I**). The investigated spinel lherzolite (sample KLA1736A) is protogranular with olivine, orthopyroxene, and clinopyroxene porphyroclasts (<5 mm). Deformation lamellae, subgrains, and undulose extinction in many olivine and orthopyroxene grains indicate intracrystalline deformation, but local recovery is shown by domains with prevailing mosaic texture. Locally, patches of small olivine + clinopyroxene + colorless silicic glass ± spinel ± phlogopite have replaced orthopyroxene. Spinel (<0.6 mm in size, up to 3 vol%) occurs in all xenoliths and commonly has a corona of phlogopite ± amphibole. Fluid and melt inclusions occurring within groups or along trails that commonly cut grain boundaries are ubiquitous.

Many peridotite xenoliths contain one or more veins or veinlets of phlogopite + clinopyroxene ± amphibole ± spinel ± glass (**Figure 2G**). Veins can be irregularly shaped, and commonly show zonations in modal composition and/or grain size along their length and also in cross section. Locally, the contact between peridotite olivine and vein phlogopite or

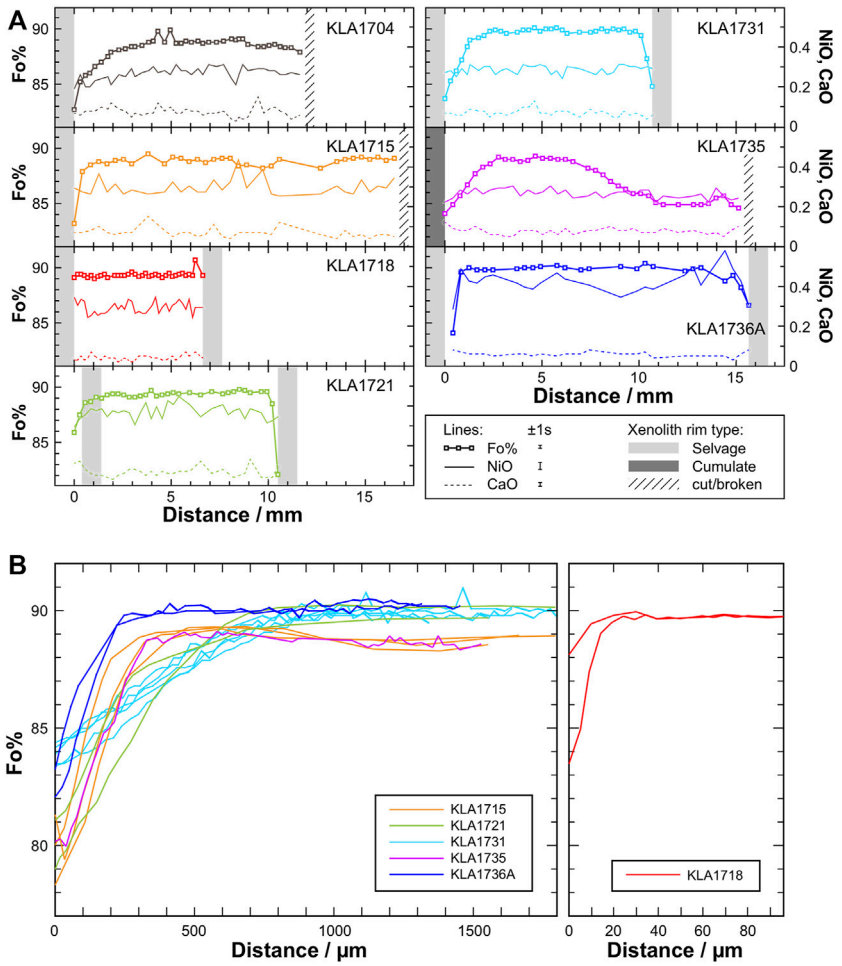

FIGURE 6 | (A) Zonations in forsterite content (Fo%; lines with symbols), NiO (without symbols) and CaO (dashed lines) of olivines across the investigated peridotite xenoliths. Scale on left side of each plot is for Fo%, right side for NiO and CaO in wt%. Error bars in legend indicate analytical uncertainty (±1 standard deviation). Note that most xenoliths show a plateau of broadly constant composition in their central part. **(B)** Zonations in Fo% at the rims of the peridotite xenoliths. The gradual decrease in Fo% extends over 0.3–1.6 mm length, except for sample KLA1718 where gradients are only 0.03–0.04 mm wide.

amphibole is characterized by a reaction zone of fine-grained clinopyroxene. The veins partly resemble the thin "phlog veins" and the broader "phlog-amph veins" and "amph veins" described in detail for basanite-hosted peridotite xenoliths from La Palma (Wulff-Pedersen et al., 1999).

Rare composite xenoliths consist of peridotite fragments and amphibole-clinopyroxene dominated cumulates. In one sample studied here (KLA1735) a wehrlite fragment adjoins a cumulate dominated by oikocrysts of kaersutitic amphibole with euhedral to anhedral olivine, clinopyroxene, and opaques (**Figure 2G**). At the contact to the cumulate, the wehrlite has a reaction rim of clinopyroxene with subordinate magnetite. The cumulate differs from the kaersutitite xenoliths described above by its poikilitic texture and the presence of olivine, and apparently has no direct genetic relationship to the host tephriphonolite. Some veins cut through both the wehrlite and kaersutitite, indicating that they formed by a separate event after cumulate crystallization. Such composite xenoliths are not restricted to the tephriphonolite studied here, but also occur in basanites from Cumbre Vieja (Klügel, 1998; Klügel et al., 2005).

The composition of olivine is $Fo_{88.5\text{-}90.5}$ in the peridotite xenoliths' interior and in most cases shows little variation, except for the strong internal zonation of composite xenolith KLA1735 (**Figure 6A**). Towards the xenoliths' rims and selvages the forsterite content decreases strongly (see below). NiO in the xenolith interior mostly varies between 0.25 and 0.40 wt%, but is higher in the spinel lherzolite KLA1736A (0.30–0.55 wt%). CaO is mostly <0.1 wt% (**Figure 6A**). Peridotite clinopyroxene is diopside with a Mg# of 86–94 and high contents of Cr_2O_3 (0.1–3.0 wt%) and Na_2O (0.4–2.1 wt%), but poor in Al_2O_3 (<2 wt%) and TiO_2 (<1 wt%). Clinopyroxene in veins has similar compositions but a tendency to lower Mg# (84–91; **Figure 7A**). Orthopyroxene of the lherzolite sample is enstatite with a Mg# of 90–91. Peridotite spinel is magnesiochromite and chromite with a Cr# (=molar Cr/

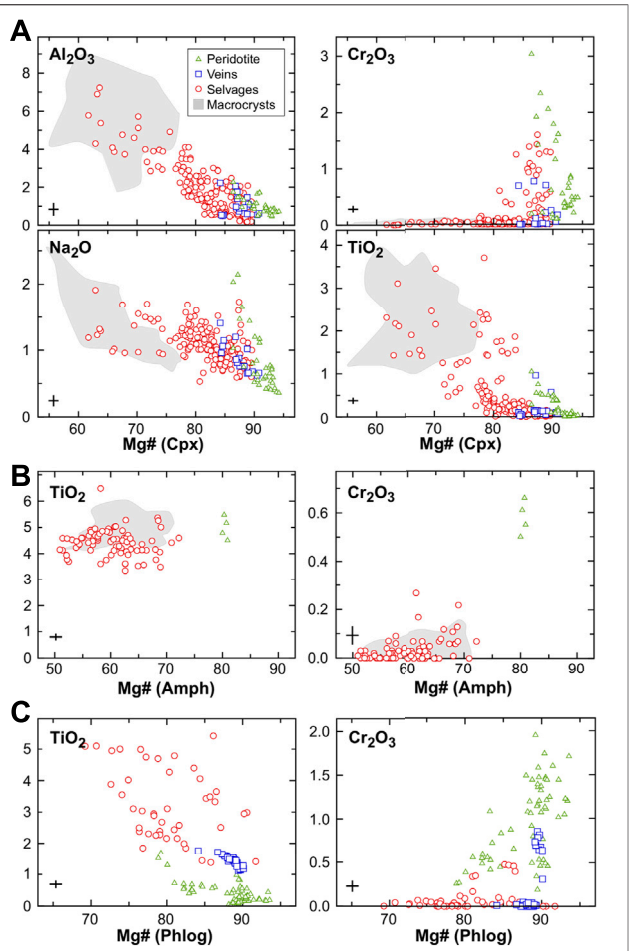

FIGURE 7 | Chemical compositions of **(A)** clinopyroxene, **(B)** amphibole, and **(C)** phlogopite in peridotite xenoliths with their selvages and veins. Peridotite clinopyroxene refers to larger grains in samples with a cumulate-like texture. Gray fields mark the range for clinopyroxene and amphibole macrocrysts in the host tephriphonolite. Error bars indicate analytical uncertainty (±1 standard deviation) as based on the analyses of secondary standards.

(Cr+Al)*100) of 56–96 and low TiO_2 (<2.8 wt%). Phlogopite has Mg# of 79–93, comparatively high Cr_2O_3 (0.2–2.0 wt%), and low TiO_2 (<1.7 wt%); vein phlogopite has a tendency to higher TiO_2 and lower Cr_2O_3 (**Figure 7C**). Amphibole has Mg# around 80, 0.5–0.7 wt% Cr_2O_3, 4.5–5.5 wt% TiO_2, and little variation in CaO, Na_2O and K_2O.

Selvages and Zonations at Peridotite Xenolith Rims

The contact between xenolith olivines and host tephriphonolite is marked by polycrystalline zoned selvages of variable composition and thickness. They cut pre-existing structures and have sharp to convoluted contacts to olivine, and can show considerable textural variation along their length. A selvage typically comprises three parts (**Figures 2F,H**): *1*) a 0–1 mm thick inner reaction rim (termed *rim I*) consisting of fine-grained clinopyroxene + Ti-magnetite ± amphibole ± phlogopite ± glass, commonly with symplectitic texture; *2*) a 0–3 mm thick central zone (termed *rim II*) consisting of phlogopite ± fine-grained clinopyroxene + Ti-magnetite ± olivine ± glass; and *3*) an up to 5 mm thick outer part with cumulus texture (termed *cumulate zone*) consisting of euhedral to subhedral amphibole ± clinopyroxene ± Ti-magnetite ± apatite ± glass. Not all selvages show these three parts; in some samples either rim I or rim II are missing locally or entirely (**Figure 2I**). Phlogopite and amphibole in selvages are locally opacitized and almost opaque. The selvages resemble those commonly present around basanite-hosted peridotite xenoliths from La Palma (Klügel, 1998, 2001), but the latter are typically thinner and lack the phlogopite-rich rim II. The inner selvage (rim I) also has similarities to rims formed by experimental reactions between olivine and evolved melts (Coombs and Gardner, 2004; Grant et al., 2014a).

Clinopyroxene in selvages is compositionally variable (Mg# 62–89), grading from peridotite clinopyroxene-like near the olivine contact in rim I to host macrocryst-like towards the cumulate zone (**Figure 7A**). Similar variations are seen in the inner and outer selvage parts of basanite-hosted peridotite xenoliths (Klügel, 1998, 2001). Amphibole in selvages largely overlaps with host macrocryst composition (Mg# 52–72), but with a tendency to lower TiO_2 (**Figure 7B**). Phlogopite in selvages show almost no compositional overlap with that within the peridotites, being distinguished by lower Cr_2O_3 (<0.5 wt%), higher TiO_2 (1.4–5.4 wt%), and a tendency to lower Mg# (69–91) (**Figure 7C**).

All peridotite xenoliths show a prominent zonation in olivine compositions towards their rims. Typically, the forsterite content decreases steadily from Fo_{88-91} in the xenolith interior to Fo_{78-86} at the selvage boundary over a distance of between 0.3 and 1.6 mm; this distance can vary within a single sample (**Figure 6B**). An exception is sample KLA1718 with much shorter gradients of 0.03–0.04 mm. The selvage of this sample is also significantly thinner (80–200 μm) than at most other samples and lacks rim I, with rim II consisting of microcrystalline phlogopite. The Fo% zonations at xenolith rims are continuous across grain boundaries and are not accompanied by textural changes of the olivines. There is no textural evidence for late olivine growth towards the selvages; rather, olivine was partly consumed during selvage formation. The shape of the Fo% zonations can show irregularities in the vicinity of veins and fine-grained phlogopite-rich aggregates. The zonations are commonly accompanied by decreasing NiO, and increasing CaO and MnO, towards the selvages. The NiO and CaO gradients are shorter than the Fo% zonations, whereas MnO follows FeO. In some compositional profiles NiO and CaO show irregular zonation, and/or strong inflections near veins and fine-grained phlogopite-rich aggregates.

Similar zonations occur at almost every basanite-hosted peridotite xenolith from Cumbre Vieja investigated by us, and were termed diffusion zones in previous studies (Klügel et al., 1997; Klügel, 1998, 2001). The width of the zones (i.e., the length of the Fo% gradient in olivine) ranges between 0.9 and 2.6 mm. Klügel (1998, 2001) argued why

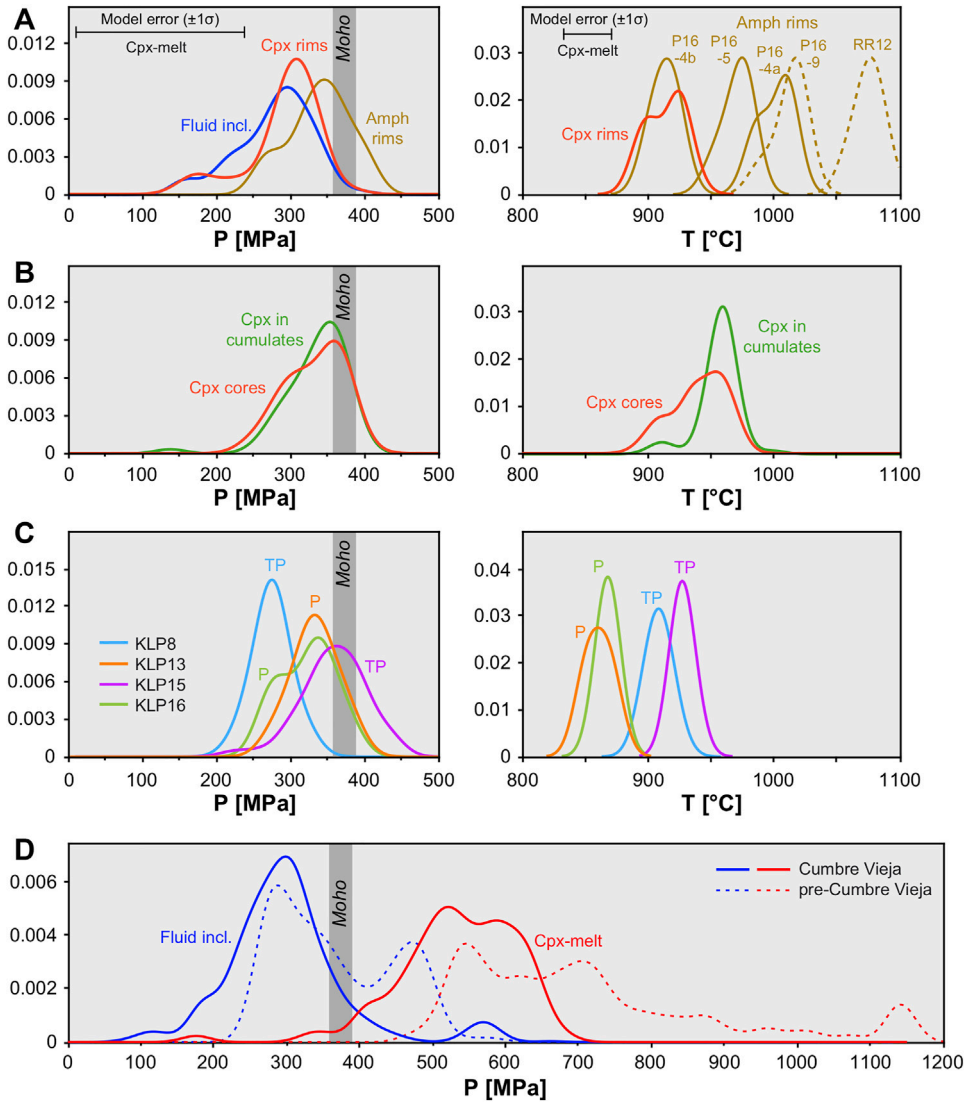

FIGURE 8 | Thermobarometric data displayed as kernel density estimates using bandwiths of 20 MPa for pressure and 10°C for temperature. A sample represents a single fluid inclusion or mineral rim analysis in **(A–C)**, and the mean rim composition of a single crystal in **(D)**. Gray bars show the estimated pressure at Moho depth around La Palma (Ranero et al., 1995). **(A)** Left: Pressure estimates for tephriphonolite macrocryst rims derived from clinopyroxene-melt barometry (red line; model Palk2012 of Masotta et al., 2013), amphibole-melt barometry (brown line; Eq. 7a of Putirka, 2016), and fluid inclusion barometry (blue line). Right: Temperature estimates for the same samples derived from clinopyroxene-melt thermometry (red line; model Talk2012 of Masotta et al., 2013), amphibole-melt thermometry (brown solid lines; Eqs 4a, 4b and 9 of Putirka, 2016), and amphibole-only thermometry (brown dashed lines; Ridolfi and Renzulli, 2012; Eq. 5 of Putirka, 2016). All rim analyses were paired with host groundmass analyses. **(B)** Pressure and temperature estimates for tephriphonolite macrocryst cores and cumulate xenolith crystals derived from clinopyroxene-melt thermobarometry, using the models Palk2012 and Talk2012 of Masotta et al. (2013). All clinopyroxene analyses were paired with suitable whole-rock compositions from Cumbre Vieja (*see* text for details). **(C)** Pressure and temperature estimates for other Cumbre Vieja tephriphonolites (TP) and phonolites (P) derived from clinopyroxene-melt thermobarometry (models Palk2012 and Talk2012 of Masotta et al., 2013). **(D)** Pressure estimates for basalts from Cumbre Vieja (solid lines) and from pre-Cumbre Vieja series (dashed lines), obtained by clinopyroxene-melt barometry on phenocryst rims, and by fluid inclusion barometry (data from compilation in Klügel et al., 2015).

these zones are best explained by diffusive Fe-Mg exchange with mafic melt across the xenolith rims and selvage, and showed that a slight s-shape of some profiles can reflect changing boundary conditions, such as decreasing diffusivity through the selvage. Diffusive exchange can also account for zonations in olivines next to veins (Wulff-Pedersen et al., 1996). By analogy, we propose that the Fo% zonations at the rims of tephriphonolite-hosted peridotite xenoliths have formed in a similar manner.

Geothermobarometry and Hygrometry

Clinopyroxene-Based Thermobarometry

Clinopyroxene-melt equilibria provide a reliable thermometer and the probably most sensitive and accurate mineral-based

barometer (Putirka, 2008). Clinopyroxene-melt thermobarometers that are universally applicable were calibrated on a wide compositional range of experimental liquids (Putirka et al., 1996, 2003; Putirka, 2008), but do not perform well for tephriphonolitic to phonolitic liquids, as these were poorly represented in the experimental data. Masotta et al. (2013) calibrated clinopyroxene-melt thermobarometers specifically for evolved alkaline liquids, which are similar to the groundmass compositions of our study. To constrain pre-eruptive pressure (P) and temperature (T) of the phonolitic melts, we applied the models Palk2012 and Talk2012 of Masotta et al. (2013) to compositions of euhedral macrocryst rims and host groundmass, assuming that the groundmass is the best approximation of the intratelluric melt (**Supplementary Table S6**). Crystal rims were analyzed at ~5 µm distance to planar surfaces. The crystal-melt compositional pairs thus have a well-defined petrographic relationship, and texturally indicate near equilibrium conditions, albeit not necessarily chemical equilibrium. Melt H_2O content was set to 3 wt% based on data from melt inclusions in Cumbre Vieja cumulates (Parat et al., 2011). We note that the dependence of the thermobarometer results on melt H_2O is rather small with −5°C/wt% and +7 MPa/wt%, respectively. The standard error of estimate (SEE) for the thermobarometer is 18°C and 115 MPa, respectively. As chemical equilibrium test, we used 1) $\Delta K_D(Fe\text{-}Mg)^{cpx-liq}$ (hereafter ΔK_D), the difference between the measured Fe-Mg distribution coefficient and that predicted by equation 35alk of Masotta et al. (2013), and 2) ΔDiHd, the difference between measured and predicted diopside-hedenbergite component in clinopyroxene (after Mollo et al., 2013). ΔDiHd is a more robust equilibrium filter than ΔK_D (Mollo et al., 2013), but is not well calibrated for evolved alkaline melts. Both ΔK_D and ΔDiHd should be < 0.1 and <0.12, respectively, corresponding to 2 SEE of the prediction equations.

For the xenolith-rich tephriphonolite, 58 rim analyses of 11 clinopyroxene macrocrysts in two samples give pressures of 297 ± 49 MPa and temperatures of 912 ± 14°C (average and one standard deviation indicated). Kernel density estimates (KDE) show well-defined maxima around 300 MPa and 920°C, respectively (**Figure 8A**). Despite evidence of sector zonations in clinopyroxene rims (**Figure 3B**) the P-T results show limited scatter; pressures <200 MPa are indicated only by few analyses with low Al_2O_3 and high SiO_2. The ΔK_D filter would remove more than half of the data pairs, with little change in pressure KDE and average (270 ± 59 MPa), and no change in temperature. The ΔDiHd filter would have negligible effect, because most data pairs are in the equilibrium range. The clinopyroxene components EnFs and Jd (Putirka, 1999) also show good agreement between measured and predicted values. For these reasons we did not discard any mineral-melt pair. Tentative application of the Putirka et al. (2003) thermobarometer yields 762 ± 139 MPa and 887 ± 20°C for the xenolith-rich tephriphonolite. The pressure estimates show large scatter and are higher than those for basanites and tephrites from Cumbre Vieja (**Figure 8D**), which appears petrologically questionable. This discrepancy corroborates the usage of a specific thermobarometer calibration for evolved alkaline melts.

For clinopyroxene-melt barometry on macrocryst cores and cumulate crystals, the melt composition is basically unknown. We tentatively applied a two-step liquid-matching approach to each clinopyroxene analysis, using a set of ca. 260 published whole-rock compositions from Cumbre Vieja (data sources as in **Figure 4**). In the first step the melts were screened for $K_D(Fe\text{-}Mg)^{cpx-liq}$ to judge whether the thermobarometer calibrations for evolved liquids (Masotta et al., 2013) or primitive to intermediate liquids (Putirka et al., 2003; Putirka, 2008) were appropriate. As all clinopyroxene analyses are best paired with rather evolved melts, we exclusively used the Masotta et al. (2013) models. In the second step we selected all melts that could have been in chemical equilibrium with a given clinopyroxene analysis. As equilibrium filter we used ΔK_D and ΔDiHd as described above, and discarded all melts with <52 wt SiO_2. Between two and 53 putative equilibrium melts passed this filter for any clinopyroxene analyzed; all crystal-melt pairs additionally show agreement between measured and predicted EnFs and Jd components (Putirka, 1999). We then calculated pressure and temperature for each of these melts, and averaged the results to obtain a single P-T estimate. The standard deviations for each P and T estimate so obtained were in the range 34–79 MPa and 11–42°C, respectively (**Supplementary Table S6**).

The inner regions of clinopyroxene macrocrysts from the xenolith-rich tephriphonolite give pressures of 332 ± 39 MPa and temperatures of 941 ± 21°C; KDE curves show maxima around 350 MPa and 950°C, and subordinate maxima around 300 MPa and 910°C. Clinopyroxenes in cumulate xenoliths give 335 ± 42 MPa and temperatures of 956 ± 15°C, overlapping almost perfectly with the macrocryst data (**Figure 8B**). The data distributions essentially overlap with those for clinopyroxene rims, with a slight shift to higher pressure and temperature (**Figure 8A**). The results are to be viewed critically because best-matching melt compositions are not necessarily close to true ones. However, the low dispersion of the data lends credibility to this approach.

Comparison With Other Tephriphonolites and Phonolites From Cumbre Vieja

In order to compare the xenolith-rich tephriphonolite to other evolved Cumbre Vieja rocks in terms of composition and thermobarometric data, we analyzed whole-rock, groundmass and clinopyroxene macrocryst compositions of four additional tephriphonolites to phonolites (samples KLP-8, -13, -15, -16; **Supplementary Table S1**). The macrocryst phases of these rocks are plagioclase + kaersutite + clinopyroxene + Ti-magnetite ± apatite ± titanite; small cumulate aggregates of these phases are common. Their groundmasses are feldspar-dominated and have phonolitic compositions, overlapping with the tephriphonolite from this study. As the groundmass compositions are very similar (**Figure 4**), differences in whole-rock compositions are largely due to the strongly different macrocryst cargos.

Clinopyroxene-melt thermobarometry applied to macrocryst rims and groundmass compositions yields pressures of 229–446 MPa and temperatures of 849–937°C; the respective KDE maxima are in the range 280–360 MPa and 860–930°C (**Figure 8C**). Measured and predicted $K_D(Fe\text{–}Mg)^{cpx-liq}$ agree

within 2 SEE for almost all data pairs. Whereas the pressure distributions overlap strongly and show no systematic dependency on sample type, temperatures for tephriphonolites are some tens of degrees higher than for phonolites, as is petrologically reasonable. Tentative application of the Putirka et al. (2003) thermobarometer gives mean pressures of 815, 930, 641 and 1,153 MPa for samples KLP-8, -13, -15, and -16, respectively, which appear unrealistically high.

Amphibole-Based Thermobarometry

Amphibole composition and amphibole-melt equilibria provide valuable thermometers but have limited potential for barometry, in particular at low pressures (e.g., Shane and Smith, 2013; Erdmann et al., 2014; Putirka, 2016). We used thirteen rim analyses of kaersutite macrocrysts in two tephriphonolite samples and applied the amphibole-only thermobarometer of Ridolfi and Renzulli (2012) (abbreviated as RR12), as well as the pressure-independent thermometers of Putirka (2016) (abbreviated as P16) based on Na partitioning (Eq. 4a), Ti partitioning (Eq. 4b), Na-K exchange (Eq. 9), and amphibole composition only (Eq. 5). These calibrations yield strongly differing temperatures, with a total range of 895–1,089°C (**Supplementary Table S7**) and KDE maxima between 910 and 1,077°C (**Figure 8A**). The high values of RR12 (1,057–1,089°C) do not overlap with results from other thermometers, and are above the temperatures of amphibole saturation calculated by Eq. 3 of Putirka (2016) (**Supplementary Table S5**). Data analysis shows that the high temperatures are due to the pressure-dependency of RR12, in conjunction with an apparent overestimation of pressures by this calibration. The amphibole-only thermometer P16-5 also appears to overestimate temperatures for our sample suite, yet it discriminates between macrocryst rims (1,013 ± 12°C), macrocryst cores (1,040 ± 17°C), and cumulate xenolith crystals (1,057 ± 8°C) (averages and standard deviations indicated). The observed temperature decrease from core to rim is petrologically reasonable for normally zoned crystals, as is a higher temperature indicated by potentially earlier formed cumulates.

Of the different amphibole-melt thermometers, only calibration P16-4b (914 ± 9°C) shows good overlap with the clinopyroxene-melt data (913 ± 14°C); calibrations P16-4a and P16-9 differ from P16-4b by 88 and 57°C on average, respectively. This discrepancy is beyond the thermometers' prediction errors, and may be caused by chemical disequilibrium between crystal rims and liquid (i.e., host groundmass composition). Although the Fe-Mg distribution coefficient for all pairs is within the range of 0.28 ± 0.11 for experimental data, disequilibrium for Na, Al, or Ti exchange due to e.g. different closure temperatures is still possible (Putirka, 2016). Possible disequilibrium is corroborated by significant differences between the predicted SiO_2 of liquids coexisting with amphibole rims (Eq. 10 of Putirka, 2016) of 52.3 ± 1.8 wt%, and the observed values of 59.3–60.2 wt%. In addition, amphibole-thermometers applied to SiO_2-poor and Al_2O_3-rich alkaline magma series are known to overestimate temperatures (Erdmann et al., 2014). For these reasons we view the amphibole-based thermometer data with caution and prefer the clinopyroxene-melt data.

Despite the limitations of amphibole barometry, we tentatively applied Eq. 7a of Putirka (2016) to macrocryst rim and host groundmass compositions of the tephriphonolite (3 wt% H_2O in the melt) and obtained plausible results of 340 ± 42 MPa, overlapping with the clinopyroxene-melt data (**Figure 8A**). The values increase by about 50 MPa per 1 wt% increase in H_2O. In contrast, the amphibole-only barometer of Ridolfi and Renzulli (2012) gives 764 ± 130 MPa for the macrocryst rims, well above the other barometric data. This is in line with earlier studies demonstrating the limited applicability of this barometer (Erdmann et al., 2014; Putirka, 2016).

Oxybarometry

Oxygen fugacities (fO_2) were estimated from kaersutite macrocryst compositions, using the chemometric equations of Ridolfi and Renzulli (2012) calibrated for a wide compositional range. Our analyses yielded near-Gaussian frequency distributions for ΔNNO (log units above the Ni-NiO solid buffer) with averages of 2.5 ± 0.6 for macrocrysts and 1.8 ± 0.4 for cumulate xenolith crystals (**Supplementary Table S7**), indicating relatively oxidizing conditions. We note, however, that the results are slightly beyond the T-fO_2 range used for the Ridolfi and Renzulli (2012) calibration. Moreover, Erdmann et al. (2014) found that the reliability of this oxybarometer is worse than that of the Ridolfi et al. (2010) calibration, which is however calibrated for calc-alkaline magmas only. Our tentative application of the Ridolfi et al. (2010) model yielded ΔNNO values of −0.5 ± 0.3 for both macrocrysts and cumulate xenolith crystals.

In addition we calculated fO_2 from Fe_2O_3/FeO ratios in evolved Cumbre Vieja rocks (>50 wt% SiO_2), using 58 whole-rock analyses in which FeO was determined by potentiometric titration (Hernandéz-Pacheco and De la Nuez, 1983; Carracedo et al., 2001; Praegel and Holm, 2006). Molar Fe_2O_3/FeO of these analyses encompass a considerable range with an average of 0.77 ± 0.32. Following Kress and Carmichael (1991) we obtain average ΔNNO values of 3 ± 1.1. This is in good agreement with the Ridolfi and Renzulli (2012) model applied to our amphibole analyses, considering that whole-rock Fe_2O_3/FeO ratios provide an upper limit for fO_2 due to possible oxidation during and after magma emplacement. The combined data suggest that the crystallization conditions of the tephriphonolite were relatively oxidizing with about two–three log units above the NNO buffer. These oxidizing conditions are consistent with the presence of haüyne in the samples, which requires fO_2 significantly above NNO (Berndt et al., 2001).

Plagioclase-Liquid Hygrometry

In order to obtain a direct estimate for the H_2O content of the studied tephriphonolite samples, we applied the plagioclase-liquid hygrometer of Waters and Lange (2015) to the compositions of groundmass and plagioclase macrocrysts (An_{30-46}). This hygrometer was calibrated with a wide range of melt compositions including mafic alkaline melts, and has a SEE of 0.35 wt% H_2O. For a P-T range of 200–400 MPa and

900–950°C as input (cf. **Figure 8**) we obtained H_2O concentrations between 2.8 and 4.0 wt%. The calculated H_2O contents are essentially independent of pressure, and are in agreement with melt inclusion data in Cumbre Vieja cumulates (Parat et al., 2011). The hygrometer after Ridolfi and Renzulli (2012) applied to kaersutite macrocrysts yields slightly higher H_2O contents of 4.0–4.6 wt%, but these estimates should be treated with caution (Erdmann et al., 2014; Putirka, 2016). For comparison, H_2O contents of Cumbre Vieja basanites that fractionate in the upper mantle were inferred to be 0.8–1.5 wt% (Weis et al., 2015).

Microthermometry

Fluid inclusions are ubiquitous in peridotite and gabbro xenoliths, occurring as trails that can crosscut grain boundaries (secondary inclusions), or randomly in small groups (primary inclusions, cf. Roedder 1984). Fluid inclusions are less common in peridotite xenolith selvages, cumulate xenoliths and macrocrysts; in these cases they occur mostly as single primary inclusions. In order to constrain pressures of inclusion formation or re-equilibration, we investigated primary and secondary fluid inclusions in peridotite olivines (N = 43), kaersutite and clinopyroxene macrocrysts (N = 5), and clinopyroxenes from peridotite selvages (N = 20) by microthermometry (**Supplementary Table S11**).

The investigated inclusions froze to solid CO_2 and vapor during cooling between −80 and −100°C; further cooling to −190°C did not yield additional phase transitions. During reheating, the inclusions showed a melting point between −56.9 and −56.4°C, close to the triple point of pure CO_2 (−56.6°C); no melting interval was observed. The investigated fluid inclusions hence consist of nearly pure CO_2, because significant amounts of additional components would have caused a melting interval with initial melting below −56.6°C (Andersen and Neumann 2001; Frezzotti et al., 2002). As no evidence for H_2O was found in any inclusion observed, it is possible that diffusive H_2O loss had occurred (Hansteen and Klügel, 2008). Upon further heating, all inclusions homogenized into the liquid phase at temperatures between 20.0 and 31.1°C; some inclusions showed critical homogenization behavior. Different microthermometric behavior of primary and secondary inclusions was not recognized, but inclusions in peridotite olivines have a tendency to lower homogenization temperatures, and hence higher densities, than inclusions in selvage clinopyroxenes and macrocrysts. Similar observations were made for fluid inclusions in volcanic rocks from other localities and were assigned to olivine being less prone to re-equilibration than clinopyroxene (Hansteen et al., 1998; Galipp et al., 2006).

Densities of CO_2 inclusions as calculated from measured homogenization temperatures are 0.59–0.77 g/cm³ for peridotite olivines and 0.47–0.72 g/cm³ for selvage clinopyroxenes and macrocrysts. The data for both groups are slightly skewed towards lower densities, which probably reflects volumetric re-equilibration during ascent of the host magma. Pressures of formation or re-equilibration of the inclusions were derived from calculated isochores (Sterner and Pitzer, 1994), using a model temperature of 950°C as based on our thermometry data. The results indicate 200–400 MPa for peridotite olivines and 160–340 MPa for selvage clinopyroxenes and macrocrysts, with averages of 300 and 260 MPa, respectively. These values generally represent lower limits for the trapping pressures of the inclusions, because re-equilibration processes tend to reduce their densities. The influence of model temperature on calculated pressures is almost negligible with about 14 MPa per 50°C increase or decrease. The KDE curve overlaps remarkably well with that for clinopyroxene-melt barometry (**Figure 8A**). It also overlaps with pressure distributions derived from fluid inclusions in basalt-hosted peridotite xenoliths and macrocrysts from La Palma (**Figure 8D**).

Diffusion Modelling of Peridotite Zonations

The time scale to form the rim zonations of peridotite xenoliths (**Figure 6B**), hereafter termed diffusion zones, may be roughly assessed by a simple one-dimensional diffusion model for an infinite half space (Crank, 1975), because the profile depth is short compared to xenolith size. Boundary conditions: peridotite olivine has constant composition C_{core} initially, and at time t = 0 is brought into contact with a source (melt reservoir) of constant Mg# that is in equilibrium with a less magnesian olivine composition C_{rim}. Subsequent Fe-Mg exchange between olivine and melt across a spatially fixed interface at x = 0, and Fe-Mg interdiffusion perpendicular to the interface with constant diffusion coefficient D_{FeMg}, produce the olivine zonations observed. The diffusion equation for composition C at distance x and time t is:

$$(C - C_{rim})/(C_{core} - C_{rim}) = \mathrm{erf}\left[x \Big/ \left(2\sqrt{D_{FeMg}t}\right)\right]$$

This simplified model neglects the formation of a selvage and possible changes in melt composition and temperature over time, both of which influence shape and length of the zonation (cf. Klügel, 1998; Costa et al., 2008). The diffusion time (t) was obtained from the best fit of the measured zonations by the diffusion equation. For D_{FeMg} we used a constant value of 2.5×10^{-17} m^2s^{-1}, calculated after Dohmen and Chakraborty (2007) for T = 1,000°C, p = 300 MPa, fO_2 = NNO +1, Fo_{85} olivine, and diffusion along the [001] direction. Owing to the strong diffusion anisotropy of olivine with D_{FeMg} along [100] and [010] being 1/6 of that along [001] (Dohmen and Chakraborty, 2007), the mean D_{FeMg} for randomly orientated grains is 2/3 of that along [001]. The model temperature was tentatively chosen to be between mafic and evolved Cumbre Vieja melts (Klügel et al., 2005; **Figure 8**), because the actual melt that caused diffusion is not known. Temperature during diffusion was certainly not constant and may have varied between different xenoliths. Based on the temperature dependence of D_{FeMg} after Dohmen and Chakraborty (2007), an increase or decrease of T by 50°C would scale the calculated times by a factor of 0.49 or 2.2, respectively. Hence, the results of our modelling are only an approximation of the timescale involved in the zonations.

Calculated diffusion times for thirteen profiles in five samples range from 13 to 309 years when using the mean D_{FeMg} (**Supplementary Table S12**). Considering the diffusion

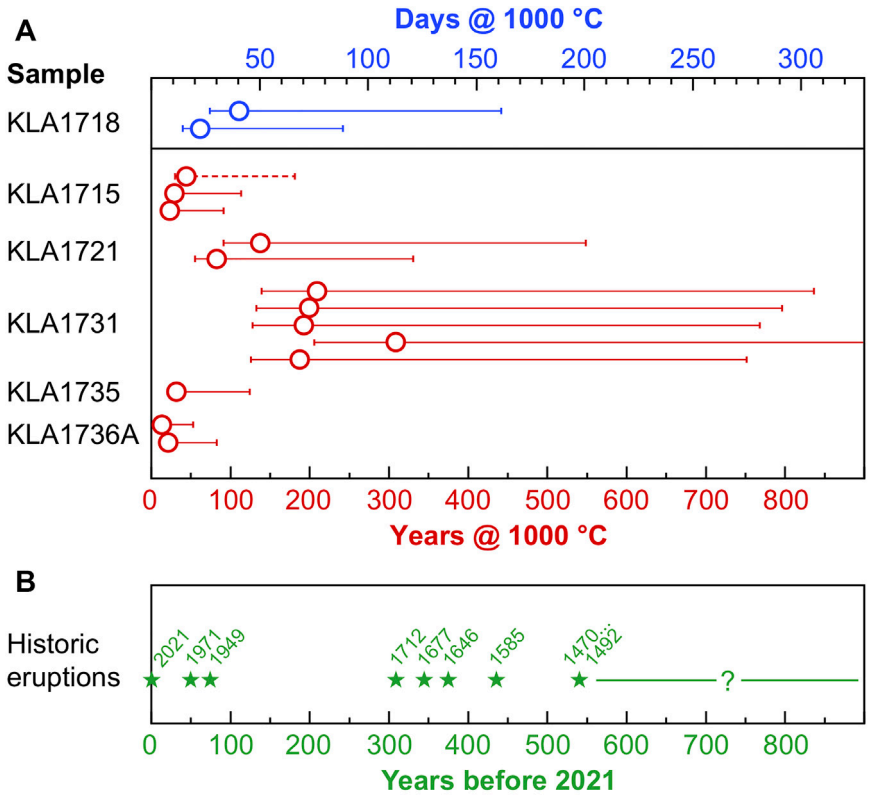

FIGURE 9 | (A) Range of diffusion times for rim zonations of the tephriphonolite-hosted peridotite xenoliths, based on a simple Fe-Mg interdiffusion model in olivine (*see* text for details). Note different scales for sample KLA1718 (blue, top) and the other samples (red, bottom). The large time range for each sample reflects the anisotropy of D_{FeMg} by a factor of six; circles mark the diffusion time for the mean D_{FeMg} of randomly orientated olivine grains (equal to 2/3 the D_{FeMg} along [001]). Diffusion times were calculated for a temperature of 1,000°C; a temperature increase or decrease by 50°C would roughly double or halve the calculated times. **(B)** The diffusion times are compared to a time line for historic eruptions on Cumbre Vieja, applying the same scale as in **(A)**. The eruption ages are summarized in Carracedo et al. (2001).

anisotropy in olivine and the unknown grain orientations in our samples, the total time range may be considerably larger (**Figure 9A**). An exception is sample KLA1718, for which a shorter range of 22–40 days for the mean D_{FeMg} is obtained (maximum range is 15–161 days); this xenolith also has an exceptionally thin selvage. The time ranges illustrated in **Figure 9A** show differences between samples that are beyond the uncertainty related to diffusion anisotropy (e.g., compare KLA1736A to KLA1731, and KLA1718 to all other samples). By considering all uncertainties of the simple diffusion model, we conclude that Fe-Mg exchange between most peridotites and surrounding melt lasted over decades to centuries, which overlaps with the time between historic eruptions on Cumbre Vieja (**Figure 9B**).

DISCUSSION

The petrographical, petrological and geochemical data of the xenolith-rich tephriphonolite provide a wealth of information on the magmatic plumbing system beneath La Palma. We now discuss the crystallization conditions of evolved magmas beneath La Palma, the timescales of their formation, the origin of the different xenolith types, and implications for phonolite generation at other oceanic island volcanoes and seamounts.

Pre-Eruptive Storage Conditions

Based on the thermobarometric and hygrometric data presented above, our best estimates of the pre-eruptive storage conditions of the xenolith-rich tephriphonolite are a pressure range of 250–350 MPa, temperature of 900–950°C, fO_2 of NNO+2 to NNO+3, and H_2O contents of 3–4 wt%. Macrocryst cores and cumulate crystals probably crystallized at slightly higher temperature but below 1,000°C (**Figure 8**). The other tephriphonolites studied here indicate similar temperatures, whereas phonolites were slightly cooler (around 830–880°C). All evolved rocks indicate essentially the same pressures, overlapping within the prediction errors of the barometers (**Figure 8C**). The pressures are equivalent to about 10–13 km depth, using a density of 2,600 kg/m^3 for the volcanic edifice and sediments and 2,900 kg/m^3 for the igneous oceanic crust. As the basement near La Palma extends from about 7 to 13 km depth (Ranero et al., 1995), this places pre-eruptive storage of evolved Cumbre Vieja magmas within the lowermost oceanic crust. This

level is not only reflected in the tephriphonolites to phonolites investigated, but is also indicated by our fluid inclusion data from macrocrysts and xenoliths in basanitic to tephritic magmas from the Cumbre Vieja (**Figure 8D**).

Our clinopyroxene-based pressure estimates are subject to considerable prediction uncertainties of the thermobarometers (**Figure 8A**), and rely on the assumption that the selected melt composition is representative of the composition at depth. For this reason, we validated our data using results from phase equilibrium experiments with evolved alkaline liquids. Of all experiments considered (Berndt et al., 2001; Freise et al., 2003; Harms et al., 2004; Andujar et al., 2008; Andujar et al., 2010; Moussallam et al., 2013; Iacovino et al., 2016), the most similar natural system is the basanite-phonolite series from Ross Island and Mt. Erebus, Antarctica. Other experimentally investigated systems are more evolved than Cumbre Vieja phonolites (Tenerife), do not fall on the Cumbre Vieja LLD (Laacher See, Kerguelen), have different phenocryst assemblages (Vesuvius, Tenerife), and/or are limited to ≤250 MPa. Our thermobarometric results are in agreement with Moussallam et al. (2013), who used Erebus phonolite to produce a phase assemblage comparable to the tephriphonolite studied by us (phonolite melt + kaersutitic amphibole + clinopyroxene + anorthoclase + Ti-magnetite) at 950°C, 100–300 MPa, fO_2 between NNO-0.8 and NNO+2.8, and 1 to 4 wt% H_2O in the melt. The crystallization of anorthoclase in the experiments rather than plagioclase as at Cumbre Vieja may reflect the more evolved bulk composition. Experiments with a Ross Island phonotephrite in the pressure range of 200–400 MPa showed that kaersutite is stable at 1,000°C for oxidized conditions (NNO+1.7 to NNO+3) and 0.7 to 4.8 wt% H_2O in the melt (Iacovino et al., 2016). Kaersutite proportions increased at higher pressure, with up to 60 wt% at 400 MPa. Their compositions overlap with those of Cumbre Vieja but extend to higher TiO_2. One important difference to the Cumbre Vieja tephriphonolite is the lack of co-existing kaersutite and clinopyroxene in the Iacovino et al. (2016) experiments, which may be due to their more primitive bulk composition. The lack of haüyne in the experiments can be ascribed to the low sulfur content of the degassed starting material. However, Moussallam et al. (2013) and Iacovino et al. (2016) found feldspar to be unstable at 250–350 MPa and 3–4 wt% H_2O. Their experimental data rather suggest that the plagioclase macrocrysts in the tephriphonolite crystallized at shallower levels and/or lower H_2O contents.

In summary, the inferred pre-eruptive storage conditions for the xenolith-rich tephriphonolite are in line with data from phase equilibrium experiments. The Moussallam et al. (2013) and Iacovino et al. (2016) experiments show that deeper fractionation levels for the tephriphonolite cannot be ruled out, because kaersutite stability extends to pressures above 400 MPa, and experiments with suitable compositions at this pressure range are lacking. On the other hand, the pressure range of 250–350 MPa inferred for the storage of the tephriphonolite is supported by the abundance of gabbro xenoliths, as these are likely derived from the lower oceanic crust (see below). The crystallization of plagioclase macrocrysts may have occurred at lower pressure, either during gradual ascent of the tephriphonolite or during temporary stagnation in the upper crust. A shallow ponding level cannot be ruled out but is not reflected in our data. The few clinopyroxene analyses indicating <200 MPa (**Figure 8A** and **Supplementary Table S6**) are not representative for the entire crystals, and may reflect limited rim growth during magma ascent.

In contrast to evolved Cumbre Vieja melts, clinopyroxene-melt barometry on basanitic to tephritic magmas indicates pre-eruptive storage and fractionation at around 450–650 MPa (Klügel et al., 2005, Klügel et al., 2015), and at deeper levels within the uppermost mantle at earlier stages of magma evolution (Barker et al., 2015). These magmas also show a bimodality of pressures derived from clinopyroxene-melt and fluid inclusion barometry, whereas the evolved magmas do not (**Figure 8**). This pressure bimodality was explained by short-term magma ponding within the lower crust during an eruption (Hansteen et al., 1998; Klügel et al., 2005). Instead of a continuous vertical ascent in a straight conduit, decompression rates must have slowed down considerably within the lower crust, either by a phase of subhorizontal flow (Klügel et al., 2015) or by slow migration through a complex storage system with limited vertical connectivity (e.g., Cashman et al., 2017). Hansteen et al. (1998) denoted this horizon in the lowermost crust as a *magma accumulation zone*, and Klügel et al. (2015) suggested that highly evolved magmas can be produced within this zone once a critical magma flux is reached. This zone was also locus of intense seismicity before and during the 2021 eruption at Cumbre Vieja (IGN, 2021).

The formation of phonolites at La Palma is not restricted to the lower crust, however. Lavas from Cumbre Vieja commonly contain reversely zoned clinopyroxene macrocrysts with green cores of low Mg# and high Na_2O, which apparently crystallized from highly evolved melts (Klügel et al., 2000). Similar green-core clinopyroxenes are found in alkaline lavas from oceanic and continental intraplate volcanoes worldwide (e.g., Duda and Schmincke, 1985; Dobosi and Fodor, 1992; Pilet et al., 2002; Leite de Oliveira et al., 2021). In many crystals, the green cores are corroded due to dissolution and/or partial melting, and the crystals can be more complexly zoned than a simple core-rim zonation. Reliable barometry on the cores is difficult since compositions of the host melts are not exactly known. However, as the brownish rims of green-core clinopyroxenes from Cumbre Vieja indicate crystallization at mantle depths (**Figure 8D**; Klügel et al., 2000, 2005; Barker et al., 2015), the green cores and the melts from which they crystallized must have formed in the mantle as well.

Provenance of the Xenoliths

Kaersutitite Cumulate Xenoliths

The mineral assemblages of kaersutitite cumulate xenoliths and the host tephriphonolite are similar, except for haüyne. Xenoliths and host also indicate similar pressures of crystallization (**Figure 8**), hence a genetic relationship between both appears likely. This relationship may be simple crystal fractionation in

which the cumulus crystals formed earlier than the host lava macrocrysts. A cognate origin of the xenoliths would agree with the predominance of kaersutite in both the cumulates and in the macrocryst assemblage of the tephriphonolite (**Figures 2A,B**). It would also be consistent with the tendency of kaersutite macrocrysts to higher Na_2O and SiO_2, and lower Al_2O_3 and TiO_2, than cumulus kaersutites with similar Mg# (**Figure 3A**), in agreement with the differentiation trend of evolved Cumbre Vieja rocks (**Figure 4**). The situation is more complicated for clinopyroxenes, however, because the effects of sector zoning are superimposed on any differentiation trend (**Figure 3B**). Yet the restriction of cumulus crystal compositions to the upper range of Mg# (mostly 67–76 for diopsides and 63–71 for kaersutites), in which they overlap with tephriphonolite macrocrysts, is in principal accordance with crystallization from the same initial magma body.

The lack of a coherent fractionation trend in **Figures 3A,B** does not rule out a direct genetic relationship between cumulates and host tephriphonolite. The scatter of the data is partly due to the presence of antecrysts and xenocrysts, as indicated by mineral zonations (**Figures 3C,D**) and by petrographic observations. In addition to kaersutite and diopside xenocrysts, some cumulate xenoliths contain olivine aggregates and single crystals that are reminiscent of mantle fragments (**Figure 2C**). The olivines had reacted with the surrounding melt to form symplectite-like reaction rims (cf. Klügel, 1998). The combined observations suggest that the early evolutionary stage of the tephriphonolite involved mixing with a magma batch from mantle depths, which introduced small mantle fragments and likely additional crystal cargo. These became part of the cumulates that were subsequently formed. In summary, our data suggest that the kaersutitite xenoliths represent cognate cumulates that formed during storage of the host tephriphonolite in a reservoir located in the lowermost crust, i.e., within the magma accumulation zone. The open cumulus texture of the xenoliths, with predominantly euhedral crystals and void space in the interstices (**Figures 2B,C**), indicates that they were not completely crystalline before eruption, but contained a considerable proportion of interstitial melt. This melt vesiculated during xenolith uplift and eruption and was squeezed out, leaving the voids now observed.

Gabbro Xenoliths From the Oceanic Crust

Gabbro xenoliths with Ti- and Al-poor clinopyroxenes are commonly found in basanites from Cumbre Vieja (e.g., Muñoz et al., 1974; Schmincke et al., 1998; Neumann et al., 2000), but to our knowledge have not been described in evolved host rocks. Based on petrography, mineral composition, and whole-rock composition, these gabbros were shown to represent fragments of the Jurassic oceanic crust underlying La Palma (Schmincke et al., 1998; Hoernle, 1998; Neumann et al., 2000). The petrographic characteristics of the tephriphonolite-hosted gabbros of our study, and the Ti-Al-poor nature of their clinopyroxenes, indicate that they are fragments of the oceanic crust as well. Like their basanite-hosted counterparts, the gabbros were metasomatized by alkaline La Palma melts und fluids migrating through the oceanic crust, which resulted in deformation, pervasive recrystallization, partial melting, and introduction of haüyne and Ti-rich amphibole (**Figures 2D,E**). Nevertheless, this late magmatic overprinting was not sufficient to obliterate the tholeiitic MORB-type character of the gabbros (Schmincke et al., 1998; Neumann et al., 2000).

According to our field observations on Cumbre Vieja, such gabbro xenoliths are second in abundance only to ultramafic cumulate xenoliths, and are particularly abundant in the terminal lavas from the 1949 eruption (Klügel et al., 1999). Their abundance is consistent with the existence of a magma accumulation zone within the lower oceanic crust. Gabbro entrainment into the tephriphonolite studied here probably occurred by diking or stoping related to its storage in the lower crust, or to the final ascent to the surface. We note that the oceanic gabbro xenoliths are clearly different from those related to crystallization of intermediate to evolved Cumbre Vieja magmas, which are termed alkaline gabbros (Klügel et al., 1999) or leucogabbros to syenites (Neumann et al., 2000; Barker et al., 2015). These are characterized by cumulus to poikilitic textures, the presence of kaersutitic amphibole ± apatite ± titanite ± haüyne in addition to plagioclase as cumulus crystals, abundant apatite inclusions in pyroxenes and amphiboles, and Ti-Al-rich clinopyroxene compositions.

Peridotite Xenoliths and Their Selvages

Peridotite xenoliths are commonly subdivided into two series, the group I or Cr-Mg series, interpreted as refractory lithospheric mantle that may or may not have been metasomatized, and the group II or Ti-Al series, interpreted as either magmatic cumulates or metasomatically overprinted group I peridotites (Frey and Prinz, 1978; Harte, 1987; Wulff-Pedersen et al., 1996). Clinopyroxenes and spinels in group I peridotites are Cr-rich and Ti-poor, and silicates generally have Mg# >85. In group II peridotites, silicates are less magnesian (Mg# <85), clinopyroxenes are augitic and Al-Ti rich, and spinels are Al-rich and Cr-poor. On La Palma, group I peridotites comprise spinel-bearing harzburgites, dunites, and minor lherzolites, whereas group II peridotites are mostly spinel wehrlites, amphibole wehrlites, and rare dunites (Wulff-Pedersen et al., 1996; Klügel, 1998; Neumann et al., 2004). These xenoliths were all interpreted to be of mantle origin, but does this also apply to the tephriphonolite-hosted peridotites of the present study?

The textures of wehrlite samples KLA1704, -1715, -1718, and -1735 are reminiscent of cumulate rocks (**Figures 2F,G**). However, similar textures can be produced by metasomatic melts that percolate through and react with mantle peridotite, crystallizing new phases that fill the melt porosity in a manner similar to intercumulus melt. Such "metasomatic infill cumulates" are texturally not necessarily distinguishable from "normal" cumulates (Harte et al., 1993). Considering mineral chemistry, clinopyroxene in the wehrlites is higher in Mg# (86–94) and Cr_2O_3, and lower in TiO_2 and Al_2O_3, than macrocrysts (**Figure 7A**). Olivine is around Fo_{89} in the xenoliths' interior (**Figure 6A**); the decrease to Fo_{85} in composite xenolith KLA1735 may reflect Fe-Mg exchange with the surrounding cumulate. Spinel is Cr-rich (Cr# 56–87) and low

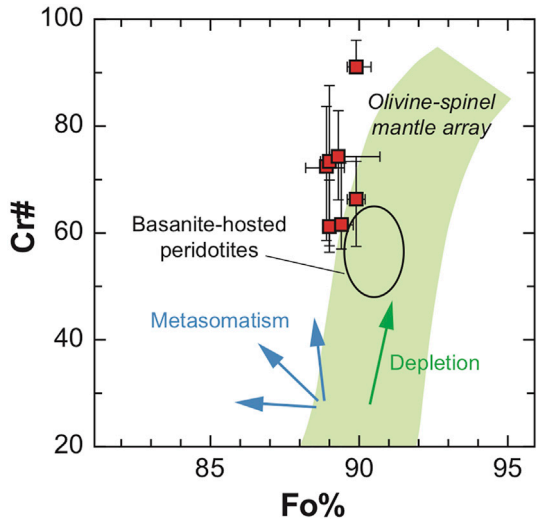

FIGURE 10 | Compositional relationship between Fo% of olivine and Cr# of coexisting spinel in the investigated peridotite xenoliths from La Palma, as compared to the mantle array after Arai (1994). Symbols indicate the average values for the interior parts of each sample; error bars encompass minimum and maximum values. Field for basanite-hosted peridotites based on data from Wulff-Pedersen et al. (1996) and Klügel (1998).

in TiO_2 (mostly <1 wt%). For these reasons the wehrlite xenoliths are unlikely to represent magmatic cumulates, but rather belong to the Cr-Mg series. They may have undergone metasomatic reactions between harzburgite and alkaline melts, leading to the dissolution of orthopyroxene (Kelemen, 1990; Kelemen et al., 1990; Wulff-Pedersen et al., 1996). Of note, Cr-Mg series wehrlite xenoliths are comparatively rare on La Palma and other Canary Islands (Neumann et al., 2004), but common in the tephriphonolite of this study. The dunite (KLA1721, -1731) (**Figures 2H,I**) and lherzolite (KLA1736A) xenoliths petrographically resemble basanite-hosted group I xenoliths from La Palma (Wulff-Pedersen et al., 1996). Their olivine (around Fo_{89-90} in the xenoliths' interior) and spinel (Cr# 57–96, TiO_2 <0.9 wt%) compositions are also consistent with a mantle origin. In a diagram of olivine Fo% versus spinel Cr#, all tephriphonolite-hosted peridotites plot at the boundary of the mantle array after Arai (1994) or slightly off it, in contrast to basanite-hosted peridotite xenoliths from La Palma (**Figure 10**). A shift to lower Fo% and/or higher Cr# likely reflects magmatic overprinting of the peridotites, consistent with the occurrence of phlogopite-clinopyroxene-amphibole veins, interstitial phlogopite, and vermicular or skeletal spinel grains (cf. Wulff-Pedersen et al., 1996, 1999; Klügel, 1998, 2001; Neumann et al., 2004).

The outer parts (cumulate zone) of the selvages encasing most peridotite xenoliths must have formed in the magma accumulation zone where the host tephriphonolite evolved, because the selvage minerals are commonly euhedral towards the host and have compositions approaching those of the macrocrysts (**Figures 7A,B**). The inner selvage parts (rims I and II) likely reflect reactions with intermediate to evolved melts not in equilibrium with forsteritic olivine. Experimental data on reactions between olivine and orthopyroxene with evolved Si-undersaturated melts show that rims some tens of microns thick can form within hours to days, growth rates decreasing strongly with increasing rim thickness (Shaw et al., 1998; Shaw, 1999; Grant et al., 2014a, 2014b). Reaction rates and type of reaction products depend on melt composition and H_2O contents. The presence of two distinct inner selvage zones in some of the peridotites studied here (clinopyroxene-rich rim I and phlogopite-rich rim II; **Figures 2F,H**) likely reflects a rapid change in xenolith environment, i.e., composition of the host melt and/or P-T conditions. Scenario 1: rim I formed within a mantle reservoir after xenolith entrainment, until a magma pulse brought the xenolith into the magma accumulation zone where rim II formed. Scenario 2: rim I and rim II both formed in the magma accumulation zone after the xenolith was brought upward by a mafic magma pulse; the break between both rims reflects injection of new magma into the evolving host melt. In either case, the complex selvages indicate contact of the xenoliths with at least two distinct melt compositions. Based on observations and results from Grant et al. (2013, 2014a, 2014b), we suggest that phlogopite-dominated rims were produced by reaction with H_2O-rich phonolitic melts, whereas clinopyroxene-rich rims indicate reaction with intermediate (tephritic to tephriphonolitic) and/or less H_2O-rich melts.

According to our diffusion modelling, the residence times of the peridotite xenoliths in alkaline magma (that is, the period between xenolith entrainment and host tephriphonolite eruption) were on the order of decades to centuries for most xenoliths (**Figure 9A**). This time scale is significantly longer than that estimated for e.g. mantle-derived fragments in the Heldburg phonolite (several months to a year; Grant et al., 2013). It also exceeds the residence times of 6–100 years calculated for basanite-hosted xenoliths from La Palma (Klügel et al., 1997; Klügel, 1998). These earlier calculations, however, assumed a rather high temperature of 1,200°C during diffusion. Considering that actual temperatures may have been close to 1,100°C (Klügel, 2001), calculated residence times may increase roughly four-fold. It thus appears that basanite- and tephriphonolite-hosted peridotite xenoliths indicate comparable residence times in alkaline magma before eruption. The effect of selvage growth on the lengths of diffusion zones was probably minor, because the selvages were highly permeable for diffusive flux of cations, and diffusion zones essentially formed after the inner reaction rims (Klügel, 2001).

To summarize, the tephriphonolite-hosted peridotite xenoliths are interpreted as mantle fragments that were metasomatized by late-stage reactions with alkaline La Palma melts. They were likely derived from the vicinity of magma reservoirs in the upper mantle decades to centuries before eruption of the host tephriphonolite. After one or more pulses of rising magma brought them into the magma accumulation zone in the lower crust, they became embedded by cumulus crystals, and selvages formed by reaction with evolving melt. The scenario of two-stage xenolith uplift is similar to that for basanite-hosted xenoliths from La Palma (Klügel, 1998), but the presence

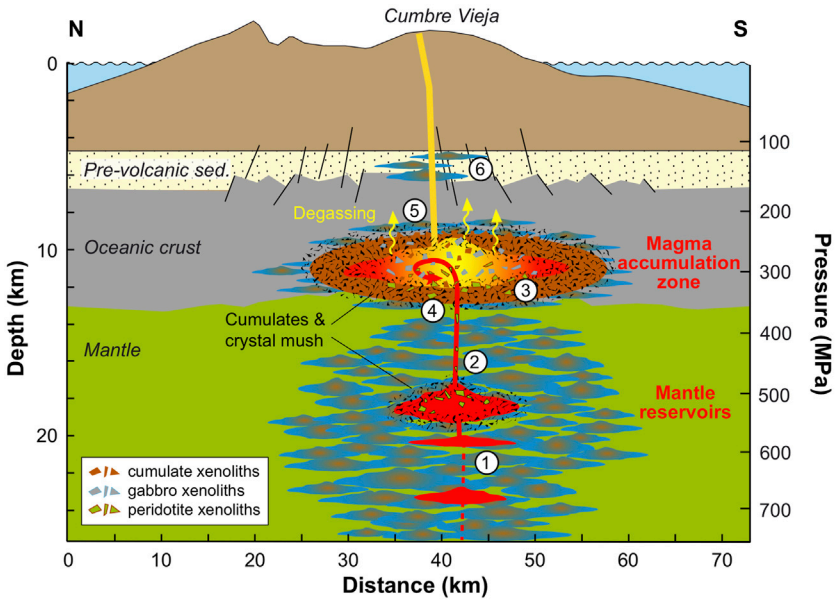

FIGURE 11 | Sketch for phonolite formation beneath La Palma. Magma reservoirs are not to scale but are enlarged to improve clarity; former melt pockets now cooled are drawn in blue, the active system in red to yellow. (1) Magmas rising from depth accumulate and fractionate to various degrees in upper mantle reservoirs. Some phonolite can form in small pockets. (2) Periodically, a reservoir ruptures and a batch of magma rises into the accumulation zone in the lower crust, in some cases carrying peridotite fragments. The magma emplacement may or may not lead to an eruption. (3) Magma in the accumulation zone continues to cool and fractionates towards phonolite. Peridotite xenoliths react with the evolved melts and become deposited in a crystal mush. Further recharge pulses bring new magma from mantle depths. (4) A final recharge event destabilizes the magma accumulation zone, causing rupture of the mafic crystal carapace and of gabbroic wall-rock, and mingling of the xenolith suite. (5) Possibly triggered by overpressurization, the tephriphonolite rises to the surface. (6) Short-term ponding in the upper crust may be possible, but is not reflected by our barometric data.

of three rather than two selvage parts in many xenoliths studied here indicates additional complexity.

Tephriphonolite Evolution and Magma Recharge

Previous studies demonstrated that phonolitic melts from Cumbre Vieja can be produced by 80–85 wt% crystal fractionation from basanitic melts (Johansen et al., 2005; Turner et al., 2015). Additional late-stage mixing with partial melts of earlier formed syenite-like rocks was invoked to explain some trace element characteristics, such as high Ba, Pb, U and Th contents of the most evolved melts (Turner et al., 2015). Our petrographic and mineral data for the xenolith-rich tephriphonolite indicate more than one mixing event. *1*) The diverse crystal cargo of the tephriphonolite and cumulate xenoliths that includes normally, reversely, or more complexly zoned clinopyroxene and kaersutite macrocrysts, partly with corroded cores, indicates magma mixing and/or incorporation of residual crystals of various origin into the evolving melt. *2*) Peridotite xenoliths with two or three distinct selvage zones indicate at least one abrupt change in host melt composition. *3*) The mineralogical variability of selvages between different peridotite xenoliths reflects contact with different alkaline melts and hence a mixed peridotite population. *4*) The large range of residence times of the peridotite xenoliths in host melts (**Figure 9A**) requires xenolith transport by more than one magma pulse. We suggest, therefore, that the petrogenesis of the tephriphonolite involved multiple recharge events in addition to crystal fractionation. The other four tephriphonolites to phonolites studied here also show diverse crystal cargos with variably zoned macrocrysts and small cumulate fragments, suggesting a similarly complex evolution as the xenolith-rich tephriphonolite, even though they lack the xenolith diversity.

Our barometric data substantiate previous suggestions (Johansen et al., 2005; Turner et al., 2015; Klügel et al., 2015) that the evolution of intermediate magmas to phonolites at Cumbre Vieja mainly occurs within a magma accumulation zone in the lower crust to Moho, whereas the more primitive magmas differentiate in the upper mantle (**Figure 11**). Magma mixing or recharge events are common in both mantle and crustal reservoirs, and are recorded as macrocryst zonations in basanites and tephrites (Klügel et al., 2000, 2005) as well as in the more evolved rocks described here. It is likely that a recharge event ultimately caused ascent and eruption of the xenolith-rich tephriphonolite. Recharge by more primitive melts is a common eruption trigger, but is not necessarily apparent in the petrological record (Rout and Wörner, 2020). The actual mechanism for ultimate destabilization and ascent of the tephriphonolite is not known. Plausible possibilities include volume increase and/or thermal disturbance induced by mixing; massive H_2O degassing due to heating by, or CO_2 flushing from, the recharge melt (Caricchi et al., 2018); and

remobilization and partial melting of older cumulates (e.g., Bachmann and Bergantz, 2008; Wolff et al., 2015).

The latest recharge into the magma accumulation zone beneath Cumbre Vieja was associated with the 2021 eruption and began some decades after the 1971 Teneguía eruption. Based on differential interferometric synthetic aperture radar (DInSAR) data, Fernández et al. (2021) inferred that already in 2009–2010 a small volume of magma moved from the mantle storage system to a depth of 8–10 km, i.e., into the accumulation zone. This resulted in fluid migration and subtle surface deformation, as well as in increased CO_2 emission at Cumbre Vieja and an increased magmatic component of helium in a cold spring 1–2 years later (Padrón et al., 2015). A similar event probably occurred in 2011–2012 (Fernández et al., 2021). The first seismic swarms indicative of volcanic unrest were recorded in October 2017 and February 2018 at mostly 15–30 km depth, and were accompanied by changes in helium and CO_2 emissions on La Palma before and after the swarms (Torres-González et al., 2020). Six further seismic swarms occurred between July 2020 and February 2021 at upper mantle depths (IGN, 2021; Longpré, 2021). From 11 September 2021 on, seismicity became more intense and shallower and was accompanied by considerable surface deformation. Hypocenters initially clustered at about 8–13 km depth, within the accumulation zone, and subsequently marked migration of magma towards the eventual eruption site, until the first vents opened on 19 September (IGN, 2021; Longpré, 2021). For the next 3 months, intense pyroclastic and effusive activity was accompanied by seismicity that clustered at about 8–16 km and 30–38 km depth.

The pre- and syn-eruptive seismicity in 2021, the analyses of the initial phase of volcanic unrest, as well as the record of mantle xenoliths from Cumbre Vieja, all indicate temporary magma ponding in the lowermost crust. This zone is periodically recharged by injection of magma from mantle reservoirs; large injections are likely to be accompanied by crustal seismicity and surface deformation. The intense pre- and syn-eruptive seismicity within the magma accumulation zone may reflect limited mobility of magma and brittle response of surrounding rock to changing pressure, as would be the case in a complex system of interconnected mush pockets or compartments (Gudmundsson, 2012; Klügel et al., 2015).

Timescales of Differentiation and Ascent

The tephriphonolite and its xenolith cargo record a succession of events that date back over centuries preceding its eruption (**Figure 9A**), which may be the timescale for differentiation of a more primitive magma to tephriphonolite. This timescale agrees with results from U-series isotope studies, indicating basanite to phonolite differentiation in 1,550–1,750 years for the Jedey phonolite of Cumbre Vieja (Johansen et al., 2005), and a few hundred to 2,000 years for Cumbre Vieja overall (Turner et al., 2015). We now compare these timescales to the recurrence rates for historic eruptions on Cumbre Vieja, which range from 22 to 237 years with an average of broadly 80 years (**Figure 9B**); this record does not take into account possible submarine eruptions. As mantle-derived magmas commonly stall during an eruption within the magma accumulation zone (Hansteen et al., 1998; Klügel et al., 2005, Klügel et al., 2015), the historic activity pattern implies new magma input into this zone every 80 years at least. This has the implication that the century-long differentiation of phonolite in the magma accumulation zone must be accompanied by a number of recharge events, provided that the passing magma batches meet the differentiating melt. In the case of the xenolith-rich tephriphonolite, it is conceivable from the data presented in **Figure 9A** that recharge may have occurred *1*) around two centuries, *2*) some decades, and *3*) some weeks prior to its eruption. These times are not well constrained, but the limited overlap of the calculated diffusion times in **Figure 9A** suggests three recharge events at least.

The timescales for final ascent of the tephriphonolite may be broadly assessed by the width of opacite rims around kaersutite macrocrysts. Experiments with andesitic to dacitic melts have shown that such amphibole reaction rims can form as a result of heating or decompression-induced H_2O degassing of the melt (Rutherford and Hill, 1993; Browne and Gardner, 2006; De Angelis et al., 2015). Both causes cannot be distinguished on the basis of rim thickness and microlite size (De Angelis et al., 2015). By applying the range of experimental growth rates to the observed rim thicknesses of 20–80 μm, we obtain reaction times of 5–102 days for decompression-induced amphibole breakdown (growth rates 9×10^{-10} to 5×10^{-9} cm/s; Browne and Gardner, 2006), and 0.1–11 days for heating-induced breakdown (3×10^{-9} to 2×10^{-7} cm/s; De Angelis et al., 2015). Data on reaction kinetics of amphibole rims in phonolitic melts are lacking, but since reaction rates increase with decreasing melt viscosity (Browne and Gardner, 2006), it is conceivable that reactions are similar or faster in less SiO_2-rich phonolites than in andesites to dacites. In summary, substantial H_2O degassing and/or heating of the tephriphonolite likely occurred days to weeks before eruption, and was possibly related to its final ascent. This timescale is comparable to the inferred diffusion time to produce the rim zonations of peridotite xenolith sample KLA1718 (**Figure 9A**), and to the timescale to form the thin phlogopite reaction rim around this peridotite (according to experimental data from Grant et al., 2014a). Entrainment of some peridotite xenoliths into the rising tephriphonolite and the formation of opacite rims around kaersutite macrocrysts thus seem to be temporally and causally related.

We suggest that the last perturbation of the differentiating tephriphonolite was a small batch of magma from depth weeks to days before eruption. The batch carried some peridotite fragments into the magma accumulation zone in the lower crust, where it mixed with a larger volume of evolved magma (**Figure 11**). However, most of the peridotite xenolith population was carried into this zone by earlier magma pulses, centuries to decades before eruption, as is indicated by diffusion times for their rim zonations (**Figure 9A**) and their thick composite selvages. The diversity of selvage compositions and the wide range of diffusion times indicate that more than one magma was involved. The peridotites carried by each pulse settled and became embedded within a mush of accumulating crystals, a scenario envisaged also for basanite-hosted xenoliths (Klügel, 1998). The last recharge may have triggered a cascade of events, including overpressurization of the magma storage system, rupture of its

mafic crystal carapace and of gabbroic wall-rock from the lower oceanic crust, entrainment of these fragments as xenoliths into the advancing magma, entrainment of peridotite fragments into the magma, and final ascent to the surface (**Figure 11**). The thorough mingling of the xenolith suite suggests a turbulent environment in the magma accumulation zone as the tephriphonolite ascended; in the conduit the viscosity was apparently high enough to prevent settling of the dense xenoliths.

Implications for Phonolite Generation at Ocean Island Volcanoes

Based on geochemical and petrological data it was proposed that the magma storage system beneath Cumbre Vieja is characterized by relatively small magma batches that differentiate in the mantle and pass the magma accumulation zone en route to the surface (Klügel et al., 2000, 2005). A similar model of magma ponding and phonolite differentiation near Moho depths was inferred for Mayotte Island, Comoros archipelago (Berthod et al., 2021). Similar storage horizons in the lower crust seem to exist beneath a number of other oceanic island volcanoes (Hansteen et al., 1998; Klügel et al., 2015), but not all of these erupt evolved magmas. For example, El Hierro Island is located next to La Palma and is of comparable subaerial age, but evolved lavas are rare and are confined to few trachyte flows and minor pyroclastic deposits (Pellicer, 1977; Carracedo et al., 2001; Pedrazzi et al., 2014). The paucity of evolved compositions at El Hierro coincides with a low eruption frequency of around 1,000 years (Becerril et al., 2016), as compared to 80 years at Cumbre Vieja. Magma supply rates are also lower for El Hierro (0.12–0.36 km^3/ka) than for Cumbre Vieja (>0.52 km^3/ka) (Carracedo, 1999; Amelung and Day, 2002). We suspect that the lower crustal magma accumulation zone under El Hierro is less mature than that under Cumbre Vieja, that is, it is cooler, smaller, and also slightly deeper as shown by barometric data (Klügel et al., 2015). In consequence, magmas stalling at this horizon receive less frequent recharge and are more prone to solidifying between recharge events, rather than evolving into trachytes or phonolites. This scenario is consistent with the precursors of the 2011–2012 El Hierro eruption, where almost 10,000 seismic events and gradual surface deformation over 3 months marked magma emplacement and dike propagation at lower oceanic crust to Moho depths (López et al., 2012; González et al., 2013; Martí et al., 2013; Domínguez Cerdeña et al., 2014), suggesting a cold and brittle environment. This contrasts with the situation at Cumbre Vieja in 2021, where intense crustal seismicity with ca. 1,400 events and surface deformation began 8 days before the eruption (IGN, 2021; Longpré, 2021).

Fogo (Cabo Verde islands) is another young volcanic oceanic island that lacks highly evolved compositions almost completely; most of the recent lavas have basanitic to phonotephritic compositions (Hildner et al., 2012, and references therein). Like Cumbre Vieja and El Hierro, Fogo is in its shield-building stage, but is more active with an average of 20 years recurrence rate of historical eruptions (Ribeiro, 1954; Day et al., 2000) and a magma supply rate of >1.7 km^3/ka (Amelung and Day, 2002). Geobarometric data for Fogo magmas strongly resemble those for Cumbre Vieja, with inferred pre-eruptive storage in the mantle at ca. 15–25 km depth, and short-term magma stalling in a magma accumulation zone in the lowermost crust at ca. 8–15 km depth (Hildner et al., 2012; Klügel et al., 2015; Klügel et al., 2020). The magma accumulation zone hence receives fresh magma from mantle reservoirs at least every 20 years on average. The frequency of these pulses keeps the accumulation zone at elevated temperatures, which may prevent significant volumes of unerupted residual melts to differentiate to phonolite. This may explain why the seismic precursors of the latest Fogo eruption in 2014 were located at shallow levels, but not in the hot lower crust where some magma may still have resided (Klügel et al., 2020).

The contrasting situations at La Palma, El Hierro and Fogo suggest that formation of significant amounts of phonolite in the magma accumulation zone in the lowermost crust is facilitated by a thermal and temporal "phonolite window." The thermal state of a storage system depends on several factors including frequency and volume of magma recharge pulses and eruptive events, and ambient temperature (e.g., Annen and Sparks, 2002). Our data for Cumbre Vieja suggest that differentiation of magma batches in the accumulation zone is accompanied by recharge events at rates similar to, or higher than, eruption rates. If recharge rates are high as at Fogo, frequent flushing of the accumulation zone may cause eruption of magma before evolved melts can form. If the rates are low as at El Hierro, unerupted melts that remain in the accumulation zone may solidify between eruptions. At Cumbre Vieja, recharge rates and volumes are balanced, such that phonolites and also intermediate compositions can form and erupt (cf. Menand, 2011). This balance may be one reason why a "Daly Gap" (Daly, 1925) is lacking at Cumbre Vieja (**Figure 4**); another reason can be partial melting of earlier intrusive rocks to produce a geochemical diversity of magmas (Annen and Sparks, 2002; Annen et al., 2006; Turner et al., 2015). Naturally, whether phonolites can form and erupt also depends on other major factors such as composition and volatile contents of the magmas, melt viscosity, storage depths of magmas, and structural regime of the volcano (e.g., Thompson et al., 2001; Gudmundsson, 2012; Andújar et al., 2013).

Sufficient magma supply provided, a magma accumulation zone in the lower crust may eventually evolve into a larger and dynamic crustal storage system that is capable of supporting explosive voluminous eruptions of evolved magma (e.g., Annen and Sparks, 2002; Menand, 2011). Long-lasting shallow storage systems are well described for comparatively thick and hot crust above subduction zones, but less so for ocean islands. The surface manifestation of such a storage system would be the dominance of phonolitic to trachytic rocks during certain evolutionary stages of an ocean island volcano, typically the late shield or post-shield stage. Examples include Brava and Santo Antão islands, Cabo Verde archipelago (Plesner et al., 2002; Holm et al., 2006; Madeira et al., 2010; Mourão et al., 2012), Tenerife and Gran Canaria, Canary Islands (Schmincke, 1976; Ablay et al., 1998; Ancochea et al., 1990, 2006), Trindade (Weaver, 1990), and Rarotonga, Cook Islands (Thompson et al., 2001). On Tenerife, experimental results indicate storage of phonolite prior to voluminous eruptions within the shallow crust, at around 50 and 130 MPa

for flank and central eruptions, respectively (Andújar et al., 2008, 2013). Assuming that phonolite magmas mainly originate by fractional crystallization of mafic magmas, differentiation of large volumes in the shallow crust alone is hardly possible due to the limited crustal space available for storage of cumulates, which can make up around 80–90% of the former melt mass (Wörner and Schmincke, 1984; LeRoex et al., 1990; Ablay et al., 1998; Johansen et al., 2005; Holm et al., 2006; Turner et al., 2015). In addition, gravimetry data for Tenerife do not indicate high density bodies below the Central Volcanic Complex that could be linked to the direct fractionation of mafic magmas at shallow levels (Gottsmann et al., 2008). Thus, a large part of crystal fractionation needs to take place at upper mantle to Moho depths, implying multi-stage differentiation (Ablay et al., 1998). By analogy to the Cumbre Vieja case, we imply that a large shallow storage system beneath an ocean island volcano is preceded by a magma accumulation zone receiving frequent magma recharge. The record of the xenolith-rich tephriphonolite studied here provides a rare opportunity to constrain the frequency of these recharge events (cf. Rout and Wörner, 2020).

CONCLUSIONS

Based on our study of a xenolith-rich tephriphonolite and other evolved rocks on Cumbre Vieja volcano, we arrive at the following conclusions:

- Storage and differentiation of evolved Cumbre Vieja magmas occur in a magma accumulation zone within the lowermost oceanic crust.
- The pre-eruptive storage conditions of a particular xenolith-rich tephriphonolite include a pressure range of 250–350 MPa, temperature of 900–950°C, fO_2 of 2–3 log units above the NNO buffer, and H_2O contents of 3–4 wt%.
- Storage and differentiation of evolved magmas are accompanied by a number of recharge events by mantle-derived mafic magmas. Recharge intervals are on the order of decades to a few centuries, comparable to eruption recurrences in historic times (80 years on average).
- Some recharge events bring mantle-derived peridotite xenoliths into the accumulation zone. Reactions between peridotite fragments and more evolved melt produce selvages around the xenoliths and diffusion zones in olivine. The xenoliths settle and become part of a crystal mush.
- The final recharge event destabilized the tephriphonolite magma in the accumulation zone some weeks prior to final ascent and eruption. This ultimately led to disruption of the surroundings of the storage horizon, entrainment of oceanic crust and cumulate fragments into the magma, and mingling of the xenolith suite during ascent.
- The occurrence of mantle xenoliths in a phonolite may be caused by recharge of mafic magma into a crustal storage system, and does not necessarily imply formation of the evolved melt in the mantle.
- Formation and eruption of phonolites at oceanic island volcanoes depend critically on the thermal regime of crust and uppermost mantle. The evolution of lower crustal storage zones is facilitated by a balance between frequency and volume of magma recharge pulses and of eruptive events. Phonolites are rare if recharge pulses occur too infrequently or too frequently.

DATA AVAILABILITY STATEMENT

The original contributions presented in the study are included in the article/**Supplementary Material**, further inquiries can be directed to the corresponding author.

AUTHOR CONTRIBUTIONS

AK and TH studied the outcrop and collected the samples, AK carried out most of the analyses and led the writing of the manuscript, and EA investigated the peridotite xenoliths and their reaction zones. All authors were actively involved in the discussion and interpretation of the data and participated in the preparation of the manuscript.

FUNDING

Our research was supported by the German Research Foundation (DFG Grant KL1313/13-1) and by department funds.

ACKNOWLEDGMENTS

We thank K. Wolff and M. Thöner (GEOMAR Kiel), B. Schulz-Dobrick and N. Groschupf (University of Mainz), B. Mader and P. Appel (University of Kiel), and S. Jung (University of Hamburg) for support of the EMP and XRF analyses, and M. N. Tubrett for the ICP-MS analyses at Memorial University of Newfoundland. We gratefully acknowledge the staff from the Unidad de Medio Ambiente on La Palma for the permission to take samples. Detailed reviews and comments by J. Andújar, A. Barker and editor M. Pichavant improved the manuscript and are gratefully acknowledged.

SUPPLEMENTARY MATERIAL

The Supplementary Material for this article can be found online at: https://www.frontiersin.org/articles/10.3389/feart.2022.761902/full#supplementary-material

REFERENCES

Ablay, G. J., Carroll, M. R., Palmer, M. R., Marti, J., and Sparks, R. S. J. (1998). Basanite-phonolite Lineages of the Teide-Pico Viejo Volcanic Complex, Tenerife, Canary Islands. *J. Petrol.* 39, 905–936. doi:10.1093/petroj/39.5.905

Amelung, F., and Day, S. (2002). InSAR Observations of the 1995 Fogo, Cape Verde, Eruption: Implications for the Effects of Collapse Events upon Island Volcanoes. *Geophys. Res. Lett.* 29 (12), 10. doi:10.1029/2001gl013760

Ancochea, E., Fuster, J., Ibarrola, E., Cendrero, A., Coello, J., Hernan, F., et al. (1990). Volcanic Evolution of the Island of Tenerife (Canary Islands) in the Light of New K-Ar Data. *J. Volcanol. Geotherm. Res.* 44 (3), 231–249. doi:10.1016/0377-0273(90)90019-C

Ancochea, E., Hernán, F., Huertas, M. J., Brändle, J. L., and Herrera, R. (2006). A New Chronostratigraphical and Evolutionary Model for La Gomera: Implications for the Overall Evolution of the Canarian Archipelago. *J. Volcanol. Geotherm. Res.* 157 (4), 271–293. doi:10.1016/j.jvolgeores.2006.04.001

Andersen, T., and Neumann, E.-R. (2001). Fluid Inclusions in Mantle Xenoliths. *Lithos* 55, 301–320. doi:10.1016/s0024-4937(00)00049-9

Andújar, J., Costa, F., and Martí, J. (2010). Magma Storage Conditions of the Last Eruption of Teide Volcano (Canary Islands, Spain). *Bull. Volcanol.* 72 (4), 381–395. doi:10.1007/s00445-009-0325-3

Andújar, J., Costa, F., Martí, J., Wolff, J. A., and Carroll, M. R. (2008). Experimental Constraints on Pre-eruptive Conditions of Phonolitic Magma from the Caldera-Forming El Abrigo Eruption, Tenerife (Canary Islands). *Chem. Geol.* 257 (3), 173–191. doi:10.1016/j.chemgeo.2008.08.012

Andújar, J., Costa, F., and Scaillet, B. (2013). Storage Conditions and Eruptive Dynamics of central versus Flank Eruptions in Volcanic Islands: The Case of Tenerife (Canary Islands, Spain). *J. Volcanol. Geotherm. Res.* 260, 62–79. doi:10.1016/j.jvolgeores.2013.05.004

Annen, C., Blundy, J. D., and Sparks, R. S. J. (2006). The Genesis of Intermediate and Silicic Magmas in Deep Crustal Hot Zones. *J. Petrol.* 47, 505–539. doi:10.1093/petrology/egi084

Annen, C., and Sparks, R. S. J. (2002). Effects of Repetitive Emplacement of Basaltic Intrusions on thermal Evolution and Melt Generation in the Crust. *Earth Planet. Sci. Lett.* 203, 937–955. doi:10.1016/s0012-821x(02)00929-9

Arai, S. (1994). Characterization of Spinel Peridotites by Olivine-Spinel Compositional Relationships: Review and Interpretation. *Chem. Geol.* 113, 191–204. doi:10.1016/0009-2541(94)90066-3

Bachmann, O., and Bergantz, G. W. (2008). Rhyolites and Their Source Mushes across Tectonic Settings. *J. Petrol.* 49 (12), 2277–2285. doi:10.1093/petrology/egn068

Barker, A. K., Rydeblad, E. M., and Silva, S. M. D. M. (2021). "Magma Storage at Ocean Islands," in *Crustal Magmatic System Evolution*. Editors M. Masotta, C. Beier, and S. Mollo (Washington, DC: American Geophysical Union), 45–78. doi:10.1002/9781119564485.ch3

Barker, A. K., Troll, V., Carracedo, J., and Nicholls, P. (2015). The Magma Plumbing System for the 1971 Teneguía Eruption on La Palma, Canary Islands. *Contrib. Mineral. Petrol.* 170 (5-6), 1–21. doi:10.1007/s00410-015-1207-7

Barker, A. K., Troll, V. R., Ellam, R. M., Hansteen, T. H., Harris, C., Stillman, C. J., et al. (2012). Magmatic Evolution of the Cadamosto Seamount, Cape Verde: beyond the Spatial Extent of EM1. *Contrib. Mineral. Petrol.* 163, 949–965. doi:10.1007/s00410-011-0708-2

Becerril, L., Ubide, T., Sudo, M., Martí, J., Galindo, I., Galé, C., et al. (2016). Geochronological Constraints on the Evolution of El Hierro (Canary Islands). *J. Afr. Earth Sci.* 113, 88–94. doi:10.1016/j.jafrearsci.2015.10.012

Berndt, J., Holtz, F., and Koepke, J. (2001). Experimental Constraints on Storage Conditions in the Chemically Zoned Phonolitic Magma Chamber of the Laacher See Volcano. *Contrib. Mineral. Petrol.* 140, 469–486. doi:10.1007/pl00007674

Berthod, C., Médard, E., Di Muro, A., Hassen Ali, T., Gurioli, L., Chauvel, C., et al. (2021). Mantle Xenolith-Bearing Phonolites and Basanites Feed the Active Volcanic ridge of Mayotte (Comoros Archipelago, SW Indian Ocean). *Contrib. Mineral. Petrol.* 176 (10), 75. doi:10.1007/s00410-021-01833-1

Bourdon, B., Zindler, A., and Wörner, G. (1994). Evolution of the Laacher See Magma Chamber: Evidence from SIMS and TIMS Measurements of U-Th Disequilibria in Minerals and Glasses. *Earth Planet. Sci. Lett.* 126, 75–90. doi:10.1016/0012-821x(94)90243-7

Browne, B. L., and Gardner, J. E. (2006). The Influence of Magma Ascent Path on the Texture, Mineralogy, and Formation of Hornblende Reaction Rims. *Earth Planet. Sci. Lett.* 246 (3-4), 161–176. doi:10.1016/j.epsl.2006.05.006

Caricchi, L., Sheldrake, T. E., and Blundy, J. (2018). Modulation of Magmatic Processes by CO2 flushing. *Earth Planet. Sci. Lett.* 491, 160–171. doi:10.1016/j.epsl.2018.03.042

Carracedo, J. C., Badiola, E. R., Guillou, H., de La Nuez, J., and Pérez Torrado, F. J. (2001). Geology and Volcanology of La Palma and El Hierro, Western Canaries. *Estudios Geológicos* 57, 175–273. doi:10.3989/egeol.01575-6134

Carracedo, J. C. (1999). Growth, Structure, Instability and Collapse of Canarian Volcanoes and Comparisons with Hawaiian Volcanoes. *J. Volcanol. Geotherm. Res.* 94, 1–19. doi:10.1016/s0377-0273(99)00095-5

Carracedo, J. C. (1994). The Canary Islands: An Example of Structural Control on the Growth of Large Oceanic-Island Volcanoes. *J. Volcanol. Geotherm. Res.* 60, 225–241. doi:10.1016/0377-0273(94)90053-1

Cashman, K. V., Sparks, R. S. J., and Blundy, J. D. (2017). Vertically Extensive and Unstable Magmatic Systems: A Unified View of Igneous Processes. *Science* 355 (6331), eaag3055. doi:10.1126/science.aag3055

Coombs, M. L., and Gardner, J. E. (2004). Reaction Rim Growth on Olivine in Silicic Melts: Implications for Magma Mixing. *Am. Mineral.* 89, 748–758. doi:10.2138/am-2004-5-608

Costa, F., Dohmen, R., and Chakraborty, S. (2008). 14. Time Scales of Magmatic Processes from Modeling the Zoning Patterns of Crystals. *Rev. Mineral. Geochem.* 69, 545–594. doi:10.1515/9781501508486-015

Crank, J. (1975). *The Mathematics of Diffusion*. London: Oxford University Press.

Daly, R. A. (1925). The Geology of Ascension Island. *Proc. Am. Acad. Arts Sci.* 60, 1–80. doi:10.2307/25130043

Day, J. M. D., Pearson, D. G., Macpherson, C. G., Lowry, D., and Carracedo, J. C. (2010). Evidence for Distinct Proportions of Subducted Oceanic Crust and Lithosphere in HIMU-type Mantle beneath El Hierro and La Palma, Canary Islands. *Geochim. et Cosmochim. Acta* 74 (22), 6565–6589. doi:10.1016/j.gca.2010.08.021

Day, S. J., Carracedo, J. C., Guillou, H., Pais Pais, F. J., Badiola, E. R., Fonseca, J. F. B. D., et al. (2000). Comparison and Cross-Checking of Historical, Archaeological and Geological Evidence for the Location and Type of Historical and Sub-historical Eruptions of Multiple-Vent Oceanic Island Volcanoes. *Geol. Soc. Lond. Spec. Publications* 171, 281–306. doi:10.1144/gsl.sp.2000.171.01.21

Day, S. J., Heleno da Silva, S. I. N., and Fonseca, J. F. B. D. (1999). A Past Giant Lateral Collapse and Present-Day Flank Instability of Fogo, Cape Verde Islands. *J. Volcanol. Geotherm. Res.* 94, 191–218. doi:10.1016/s0377-0273(99)00103-1

De Angelis, S. H., Larsen, J., Coombs, M., Dunn, A., and Hayden, L. (2015). Amphibole Reaction Rims as a Record of Pre-eruptive Magmatic Heating: An Experimental Approach. *Earth Planet. Sci. Lett.* 426, 235–245. doi:10.1016/j.epsl.2015.06.051

Devey, C. W., Lackschewitz, K. S., Mertz, D. F., Bourdon, B., Cheminée, J.-L., Dubois, J., et al. (2003). Giving Birth to Hotspot Volcanoes: Distribution and Composition of Young Seamounts from the Seafloor Near Tahiti and Pitcairn Islands. *Geology* 31, 395–398. doi:10.1130/0091-7613(2003)031<0395:gbthvd>2.0.co;2

Dobosi, G., and Fodor, R. V. (1992). Magma Fractionation, Replenishment, and Mixing as Inferred from green-core Clinopyroxenes in Pliocene Basanite, Southern Slovakia. *Lithos* 28 (2), 133–150. doi:10.1016/0024-4937(92)90028-W

Dohmen, R., and Chakraborty, S. (2007). Fe-Mg Diffusion in Olivine II: point Defect Chemistry, Change of Diffusion Mechanisms and a Model for Calculation of Diffusion Coefficients in Natural Olivine. *Phys. Chem. Mineral.* 34, 409–430. doi:10.1007/s00269-007-0158-6

Domínguez Cerdeña, I., del Fresno, C., and Gomis Moreno, A. (2014). Seismicity Patterns Prior to the 2011 El Hierro Eruption. *Bull. Seismological Soc. America* 104, 567–575. doi:10.1785/0120130200

Duda, A., and Schmincke, H.-U. (1985). Polybaric Differentiation of Alkali Basaltic Magmas: Evidence from green-core Clinopyroxenes (Eifel, FRG). *Contrib. Mineral. Petrol.* 91, 340–353. doi:10.1007/bf00374690

Edgar, C. J., Wolff, J. A., Olin, P. H., Nichols, H. J., Pittari, A., Cas, R. A. F., et al. (2007). The Late Quaternary Diego Hernandez Formation, Tenerife: Volcanology of a Complex Cycle of Voluminous Explosive Phonolitic Eruptions. *J. Volcanol. Geotherm. Res.* 160 (1), 59–85. doi:10.1016/j.jvolgeores.2006.06.001

Elliott, T. R. (1991). *Element Fractionation in the Petrogenesis of Ocean Island Basalts*. Ph.D (Milton Keynes: The Open University).

Erdmann, S., Martel, C., Pichavant, M., and Kushnir, A. (2014). Amphibole as an Archivist of Magmatic Crystallization Conditions: Problems, Potential, and Implications for Inferring Magma Storage Prior to the Paroxysmal 2010 Eruption of Mount Merapi, Indonesia. *Contrib. Mineral. Petrol.* 167 (6), 1016. doi:10.1007/s00410-014-1016-4

Fernández, J., Escayo, J., Hu, Z., Camacho, A. G., Samsonov, S. V., Prieto, J. F., et al. (2021). Detection of Volcanic Unrest Onset in La Palma, Canary Islands, Evolution and Implications. *Sci. Rep.* 11 (1), 2540. doi:10.1038/s41598-021-82292-3

France, L. (2020). Can Destabilization Rims of Hydrous Minerals Be Used to Constrain Magma Ascent Kinetics at Lava Dome Volcanoes? *Bull. Volcanol* 82 (10), 66. doi:10.1007/s00445-020-01405-4

Freise, M., Holtz, F., Koepke, J. r., Scoates, J., and Leyrit, H. (2003). Experimental Constraints on the Storage Conditions of Phonolites from the Kerguelen Archipelago. *Contrib. Mineral. Petrol.* 145, 659–672. doi:10.1007/s00410-003-0453-2

Frey, F. A., and Prinz, M. (1978). Ultramafic Inclusions from San Carlos, Arizona: Petrologic and Geochemical Data Bearing on Their Petrogenesis. *Earth Planet. Sci. Lett.* 38, 129–176. doi:10.1016/0012-821x(78)90130-9

Frezzotti, M. L., Andersen, T., Neumann, E.-R., and Simonsen, S. L. (2002). Carbonatite melt-CO2 Fluid Inclusions in Mantle Xenoliths from Tenerife, Canary Islands: a story of Trapping, Immiscibility and Fluid-Rock Interaction in the Upper Mantle. *Lithos* 64, 77–96. doi:10.1016/s0024-4937(02)00178-0

Galipp, K., Klügel, A., and Hansteen, T. H. (2006). Changing Depths of Magma Fractionation and Stagnation during the Evolution of an Oceanic Island Volcano: La Palma (Canary Islands). *J. Volcanol. Geotherm. Res.* 155, 285–306. doi:10.1016/j.jvolgeores.2006.04.002

Geldmacher, J., Hoernle, K., Bogaard, P. v. d., Duggen, S., and Werner, R. (2005). New 40Ar/39Ar Age and Geochemical Data from Seamounts in the Canary and Madeira Volcanic Provinces: Support for the Mantle Plume Hypothesis. *Earth Planet. Sci. Lett.* 237, 85–101. doi:10.1016/j.epsl.2005.04.037

González, P. J., Samsonov, S. V., Pepe, S., Tiampo, K. F., Tizzani, P., Casu, F., et al. (2013). Magma Storage and Migration Associated with the 2011-2012 El Hierro Eruption: Implications for Crustal Magmatic Systems at Oceanic Island Volcanoes. *J. Geophys. Res. Solid Earth* 118, 4361–4377. doi:10.1002/jgrb.50289

Gottsmann, J., Camacho, A. G., Martí, J., Wooller, L., Fernández, J., García, A., et al. (2008). Shallow Structure beneath the Central Volcanic Complex of Tenerife from New Gravity Data: Implications for its Evolution and Recent Reactivation. *Phys. Earth Planet. Interiors* 168 (3), 212–230. doi:10.1016/j.pepi.2008.06.020

Grant, T. B., Milke, R., Pandey, S., and Jahnke, H. (2013). The Heldburg Phonolite, Central Germany: Reactions between Phonolite and Xenocrysts from the Upper Mantle and Lower Crust. *Lithos* 182-183 (0), 86–101. doi:10.1016/j.lithos.2013.09.012

Grant, T. B., Milke, R., and Wunder, B. (2014a). Experimental Reactions between Olivine and Orthopyroxene with Phonolite Melt: Implications for the Origins of Hydrous Amphibole + Phlogopite + Diopside Bearing Metasomatic Veins. *Contrib. Mineral. Petrol.* 168, 1073. doi:10.1007/s00410-014-1073-8

Grant, T. B., Milke, R., Wunder, B., Wirth, R., and Rhede, D. (2014b). Experimental Study of Phlogopite Reaction Rim Formation on Olivine in Phonolite Melts: Kinetics, Reaction Rates, and Residence Times. *Am. Mineral.* 99, 2211–2226. doi:10.2138/am-2014-4821

Gudmundsson, A. (2012). Magma chambers: Formation, Local Stresses, Excess Pressures, and Compartments. *J. Volcanol. Geotherm. Res.* 237-238, 19–41. doi:10.1016/j.jvolgeores.2012.05.015

Hansteen, T. H., and Klügel, A. (2008). Fluid Inclusion Thermobarometry as a Tracer for Magmatic Processes. *Rev. Mineral. Geochem.* 69, 143–177. doi:10.2138/rmg.2008.69.1

Hansteen, T. H., Klügel, A., and Schmincke, H.-U. (1998). Multi-stage Magma Ascent beneath the Canary Islands: Evidence from Fluid Inclusions. *Contrib. Mineral. Petrol.* 132, 48–64. doi:10.1007/s004100050404

Harms, E., Gardner, J. E., and Schmincke, H. U. (2004). Phase Equilibria of the Lower Laacher See Tephra (East Eifel, Germany): Constraints on Pre-eruptive Storage Conditions of a Phonolitic Magma Reservoir. *J. Volcanol. Geotherm. Res.* 134, 135–148. doi:10.1016/j.jvolgeores.2004.01.009

Harte, B. (1987). "Metasomatic Events Recorded in Mantle Xenoliths: an Overview," in *Mantle Xenoliths*. Editor P. H. Nixon (Chichester: John Wiley & Sons), 625–640.:

Harte, B., Hunter, R. H., and Kinny, P. D. (1993). Melt Geometry, Movement and Crystallization, in Relation to Mantle Dykes, Veins and Metasomatism. *Philosophical Trans. R. Soc. Lond. A* 342, 1–21.

Hawkesworth, C. J., Blake, S., Evans, P., Hughes, R., Macdonald, R., Thomas, L. E., et al. (2000). Time Scales of Crystal Fractionation in Magma Chambers-Integrating Physical, Isotopic and Geochemical Perspectives. *J. Petrol.* 41 (7), 991–1006. doi:10.1093/petrology/41.7.991

Hay, D. E., and Wendlandt, R. F. (1995). The Origin of Kenya Rift Plateau-type Flood Phonolites: Results of High-Pressure/high-Temperature Experiments in the Systems Phonolite-H2o and phonolite-H2O-CO2. *J. Geophys. Res.* 100 (B1), 401–410. doi:10.1029/94jb02160

Hernandéz-Pacheco, A., and De la Nuez, J. (1983). Las extrusiones sálicas del Sur de la Isla de La Palma (Canarias). *Estudios Geológicos* 39, 3–30.

Hernandéz-Pacheco, A., and Valls, M. C. (1982). The historic eruptions of La Palma Island (Canarias). Arquipelago, Revista da Universidade dos Açores, *Série Ciencias da Natureza* 3, 83–94.

Hildner, E., Klügel, A., and Hansteen, T. H. (2012). Barometry of Lavas from the 1951 Eruption of Fogo, Cape Verde Islands: Implications for Historic and Prehistoric Magma Plumbing Systems. *J. Volcanol. Geotherm. Res.* 217-218, 73–90. doi:10.1016/j.jvolgeores.2011.12.014

Hoernle, K. (1998). Geochemistry of Jurassic Oceanic Crust beneath Gran Canaria (Canary Islands): Implications for Crustal Recycling and Assimilation. *J. Petrol.* 39, 859–880. doi:10.1093/petroj/39.5.859

Holm, P. M., Wilson, J. R., Christensen, B. P., Hansen, L., Hansen, S. L., Hein, K. M., et al. (2006). Sampling the Cape Verde Mantle Plume: Evolution of Melt Compositions on Santo Antão, Cape Verde Islands. *J. Petrol.* 47, 145–189. doi:10.1093/petrology/egi071

Iacono Marziano, G., Schmidt, B. C., and Dolfi, D. (2007). Equilibrium and Disequilibrium Degassing of a Phonolitic Melt (Vesuvius AD 79 "white Pumice") Simulated by Decompression Experiments. *J. Volcanol. Geotherm. Res.* 161, 151–164. doi:10.1016/j.jvolgeores.2006.12.001

Iacovino, K., Oppenheimer, C., Scaillet, B., and Kyle, P. (2016). Storage and Evolution of Mafic and Intermediate Alkaline Magmas beneath Ross Island, Antarctica. *J. Petrol.* 57, 93–118. doi:10.1093/petrology/egv083

IGN (2021). *Earthquake Catalogue*. Madrid: Instituto Geográfico Nacional de España. https://www.ign.es/web/ign/portal/sis-catalogo-terremotos.

Irving, A. J., and Green, D. H. (2008). Phase Relationships of Hydrous Alkalic Magmas at High Pressures: Production of Nepheline Hawaiitic to Mugearitic Liquids by Amphibole-Dominated Fractional Crystallization within the Lithospheric Mantle. *J. Petrol.* 49, 741–756. doi:10.1093/petrology/egm088

Irving, A. J., and Price, R. C. (1981). Geochemistry and Evolution of Iherzolite-Bearing Phonolitic Lavas from Nigeria, Australia, East Germany and New Zealand. *Geochim. et Cosmochim. Acta* 45, 1309–1320. doi:10.1016/0016-7037(81)90224-6

Jarosewich, E. J., Nelen, J. A., and Norberg, J. A. (1980). Reference Samples for Electron Microprobe Analysis. *Geostand. Newsl.* 4, 43–47. doi:10.1111/j.1751-908X.1980.tb00273.x

Jenner, G. A., Longerich, H. P., Jackson, S. E., and Fryer, B. J. (1990). ICP-MS - A Powerful Tool for High-Precision Trace-Element Analysis in Earth Sciences: Evidence from Analysis of Selected U.S.G.S. Reference Samples. *Chem. Geol.* 83, 133–148. doi:10.1016/0009-2541(90)90145-w

Jochum, K. P., Willbold, M., Raczek, I., Stoll, B., and Herwig, K. (2005). Chemical Characterisation of the USGS Reference Glasses GSA-1G, GSC-1G, GSD-1G, GSE-1G, BCR-2G, BHVO-2G and BIR-1G Using EPMA, ID-TIMS, ID-ICP-MS and LA-ICP-MS. *Geostand Geoanal. Res.* 29, 285–302. doi:10.1111/j.1751-908x.2005.tb00901.x

Johansen, T. S., Hauff, F., Hoernle, K., Klügel, A., and Kokfelt, T. F. (2005). Basanite to Phonolite Differentiation within 1550-1750 Yr: U-Th-Ra Isotopic Evidence from the A.D. 1585 Eruption on La Palma, Canary Islands. *Geology* 33, 897–900. doi:10.1130/g21663.1

Kelemen, P. B., Joyce, D. B., Webster, J. D., and Holloway, J. R. (1990). Reaction between Ultramafic Rock and Fractionating Basaltic Magma II. Experimental Investigation of Reaction between Olivine Tholeiite and Harzburgite at 1150-1050 C and 5 Kb. *J. Petrol.* 31, 99–134. doi:10.1093/petrology/31.1.99

Kelemen, P. B. (1990). Reaction between Ultramafic Rock and Fractionating Basaltic Magma I. Phase Relations, the Origin of Calc-Alkaline Magma Series, and the Formation of Discordant Dunite. *J. Petrol.* 31, 51–98. doi:10.1093/petrology/31.1.51

Kelly, P. J., Kyle, P. R., Dunbar, N. W., and Sims, K. W. W. (2008). Geochemistry and Mineralogy of the Phonolite Lava lake, Erebus Volcano, Antarctica: 1972-2004 and Comparison with Older Lavas. *J. Volcanol. Geotherm. Res.* 177, 589–605. doi:10.1016/j.jvolgeores.2007.11.025

Klitgord, K. D., and Schouten, H. (1986). "Plate Kinematics of the Central Atlantic," in *The Geology of North America, Vol. M, the Western North Atlantic Region*. Editors P. R. Vogt and B. E. Tucholke (Boulder, Colorado: Geological Society of America), 351–378.

Klügel, A., Day, S., Schmid, M., and Faria, B. (2020). Magma Plumbing During the 2014–2015 Eruption of Fogo (Cape Verde Islands). *Front. Earth Sci.* 8. doi:10.3389/feart.2020.00157

Klügel, A., Galipp, K., Hoernle, K., Hauff, F., and Groom, S. (2017). Geochemical and Volcanological Evolution of La Palma, Canary Islands. *J. Petrol.* 58, 1227–1248. doi:10.1093/petrology/egx052

Klügel, A., Longpré, M.-A., García-Cañada, L., and Stix, J. (2015). Deep intrusions, lateral magma transport and related uplift at ocean island volcanoes. *Earth Planet. Sci. Lett.* 431, 140–149. doi:10.1016/j.epsl.2015.09.031

Klügel, A., Hansteen, T. H., and Galipp, K. (2005). Magma Storage and Underplating beneath Cumbre Vieja Volcano, La Palma (Canary Islands). *Earth Planet. Sci. Lett.* 236, 211–226. doi:10.1016/j.epsl.2005.04.006

Klügel, A., Hansteen, T. H., and Schmincke, H.-U. (1997). Rates of Magma Ascent and Depths of Magma Reservoirs beneath La Palma (Canary Islands). *Terra Nova* 9 (3), 117–121. doi:10.1046/j.1365-3121.1997.d01-15.x

Klügel, A., Hoernle, K. A., Schmincke, H.-U., and White, J. D. L. (2000). The Chemically Zoned 1949 Eruption on La Palma (Canary Islands): Petrologic Evolution and Magma Supply Dynamics of a Rift Zone Eruption. *J. Geophys. Res.* 105 (B3), 5997–6016. doi:10.1029/1999jb900334

Klügel, A. (2001). Prolonged Reactions between Harzburgite Xenoliths and Silica-Undersaturated Melt: Implications for Dissolution and Fe-Mg Interdiffusion Rates of Orthopyroxene. *Contrib. Mineral. Petrol.* 141, 1–14. doi:10.1007/s004100000222

Klügel, A. (1998). Reactions between Mantle Xenoliths and Host Magma beneath La Palma (Canary Islands): Constraints on Magma Ascent Rates and Crustal Reservoirs. *Contrib. Mineral. Petrol.* 131, 237–257. doi:10.1007/s004100050391

Klügel, A., Schmincke, H.-U., White, J. D. L., and Hoernle, K. A. (1999). Chronology and Volcanology of the 1949 Multi-Vent Rift-Zone Eruption on La Palma (Canary Islands). *J. Volcanol. Geotherm. Res.* 94, 267–282. doi:10.1016/s0377-0273(99)00107-9

Kress, V. C., and Carmichael, I. S. E. (1991). The Compressibility of Silicate Liquids Containing Fe2O3 and the Effect of Composition, Temperature, Oxygen Fugacity and Pressure on Their Redox States. *Contrib. Mineral. Petrol.* 108, 82–92. doi:10.1007/bf00307328

Kunzmann, T. (1996). The Solidus-Liquidus Phase Relations of the Heldburg Phonolite up to 2.5 GPa. *Terra Abstr.* 8, 37–38.

Le Roex, A. P., Cliff, R. A., and Adair, B. J. I. (1990). Tristan da Cunha, South Atlantic: Geochemistry and Petrogenesis of a Basanite-Phonolite Lava Series. *J. Petrol.* 31, 779–812. doi:10.1093/petrology/31.4.779

Lechler, P. J., and Desilets, M. O. (1987). A Review of the Use of Loss on Ignition as a Measurement of Total Volatiles in Whole-Rock Analysis. *Chem. Geol.* 63, 341–344. doi:10.1016/0009-2541(87)90171-9

Leite de Oliveira, A., Costa dos Santos, A., Nogueira, C. C., Maia, T. M., and Geraldes, M. C. (2021). Green Core Clinopyroxenes from Martin Vaz Archipelago Plio-Pleistocenic Alkaline Rocks, South Atlantic Ocean, Brazil: A Magma Mixing and Polybaric Crystallization Record. *J. South Am. Earth Sci.* 105, 102951. doi:10.1016/j.jsames.2020.102951

Longpré, M.-A. (2021). Reactivation of Cumbre Vieja Volcano. *Science* 374 (6572), 1197–1198. doi:10.1126/science.abm9423

López, C., Blanco, M. J., Abella, R., Brenes, B., Cabrera Rodríguez, V. M., Casas, B., et al. (2012). Monitoring the Volcanic Unrest of El Hierro (Canary Islands) before the Onset of the 2011–2012 Submarine Eruption. *Geophys. Res. Lett.* 39 (13), 1–7. doi:10.1029/2012GL051846

Madeira, J., Mata, J., Mourão, C., Brum da Silveira, A., Martins, S., Ramalho, R., et al. (2010). Volcano-stratigraphic and Structural Evolution of Brava Island (Cape Verde) Based on 40Ar/39Ar, U-Th and Field Constraints. *J. Volcanol. Geotherm. Res.* 196, 219–235. doi:10.1016/j.jvolgeores.2010.07.010

Martí, J., Mitjavila, J., and Araña, V. (1994). Stratigraphy, Structure and Geochronology of the Las Cañadas Caldera (Tenerife, Canary Islands). *Geol. Mag.* 131 (6), 715–727. doi:10.1017/S0016756800012838

Martí, J., Pinel, V., López, C., Geyer, A., Abella, R., Tárraga, M., et al. (2013). Causes and Mechanisms of the 2011–2012 El Hierro (Canary Islands) Submarine Eruption. *J. Geophys. Res.* 118, 1–17. doi:10.1002/jgrb.50087

Masotta, M., Mollo, S., Freda, C., Gaeta, M., and Moore, G. (2013). Clinopyroxene-liquid Thermometers and Barometers Specific to Alkaline Differentiated Magmas. *Contrib. Mineral. Petrol.* 166, 1545–1561. doi:10.1007/s00410-013-0927-9

Melluso, L., Morra, V., Riziky, H., Veloson, J., Lustrino, M., Del Gatto, L., et al. (2007). Petrogenesis of a Basanite-Tephrite-Phonolite Volcanic Suite in the Bobaomby (Cap d'Ambre) peninsula, Northern Madagascar. *J. Afr. Earth Sci.* 49, 29–42. doi:10.1016/j.jafrearsci.2007.06.002

Menand, T. (2011). Physical Controls and Depth of Emplacement of Igneous Bodies: A Review. *Tectonophysics* 500, 11–19. doi:10.1016/j.tecto.2009.10.016

Middlemost, E. A. K. (1972). Evolution of La Palma, Canary Archipelago. *Contrib. Mineral. Petrol.* 36, 33–48. doi:10.1007/bf00372833

Mitchell-Thomé, R. C. (1970). *Geology of the Middle Atlantic, Beiträge zur Regionalen Geologie der Erde*. Berlin: Borntrager.

Mollo, S., Putirka, K., Misiti, V., Soligo, M., and Scarlato, P. (2013). A new test for equilibrium based on clinopyroxene-melt pairs: Clues on the solidification temperatures of Etnean alkaline melts at post-eruptive conditions. *Chem. Geol.* 352, 92–100. doi:10.1016/j.chemgeo.2013.05.026

Mortensen, A. K., Wilson, J. R., and Holm, P. M. (2009). The Cão Grande Phonolitic Fall deposit on Santo Antão, Cape Verde Islands. *J. Volcanol. Geotherm. Res.* 179, 120–132. doi:10.1016/j.jvolgeores.2008.10.014

Mourão, C., Mata, J., Doucelance, R., Madeira, J., Millet, M.-A., and Moreira, M. (2012). Geochemical Temporal Evolution of Brava Island Magmatism: Constraints on the Variability of Cape Verde Mantle Sources and on Carbonatite-Silicate Magma Link. *Chem. Geol.* 334, 44–61. doi:10.1016/j.chemgeo.2012.09.031

Moussallam, Y., Oppenheimer, C., Scaillet, B., and Kyle, P. R. (2013). Experimental Phase-Equilibrium Constraints on the Phonolite Magmatic System of Erebus Volcano, Antarctica. *J. Petrol.* 54, 1285–1307. doi:10.1093/petrology/egt012

Muñoz, M., Sagredo, J., and Afonso, A. (1974). Mafic and Ultramafic Inclusions in the Eruption of Teneguía Volcano (La Palma, Canary Islands). *Estudios Geol.*, 65–74.

Neumann, E.-R., Griffin, W. L., Pearson, N. J., and O'Reilly, S. Y. (2004). The Evolution of the Upper Mantle beneath the Canary Islands: Information from Trace Elements and Sr Isotope Ratios in Minerals in Mantle Xenoliths. *J. Petrol.* 45, 2573–2612. doi:10.1093/petrology/egh063

Neumann, E.-R., Sørensen, V. B., Simonsen, S. L., and Johnsen, K. (2000). Gabbroic Xenoliths from La Palma, Tenerife and Lanzarote, Canary Islands: Evidence for Reactions between Mafic Alkaline Canary Islands Melts and Old Oceanic Crust. *J. Volcanol. Geotherm. Res.* 103, 313–342. doi:10.1016/s0377-0273(00)00229-8

Padrón, E., Pérez, N. M., Rodríguez, F., Melián, G. V., Hernández, P. A., Sumino, H., et al. (2015). Dynamics of Diffuse Carbon Dioxide Emissions from Cumbre Vieja Volcano, La Palma, Canary Islands. *Bull. Volcanol.* 77, 1–15. doi:10.1007/s00445-015-0914-2

Parat, F., Holtz, F., and Klügel, A. (2011). S-rich Apatite-Hosted Glass Inclusions in Xenoliths from La Palma: Constraints on the Volatile Partitioning in Evolved Alkaline Magmas. *Contrib. Mineral. Petrol.* 162 (3), 463–478. doi:10.1007/s00410-011-0606-7

Pedrazzi, D., Becerril, L., Martí, J., Meletlidis, S., and Galindo, I. (2014). Explosive Felsic Volcanism on El Hierro (Canary Islands). *Bull. Volcanol* 76, 863. doi:10.1007/s00445-014-0863-1

Pellicer, M. J. (1977). Estudio volcanológico de la Isla de El Hierro, Islas Canarias. *Estudios Geológicos* 33, 181–197.

Pilet, S., Hernandez, J., and Villemant, B. (2002). Evidence for High Silicic Melt Circulation and Metasomatic Events in the Mantle beneath Alkaline Provinces: the Na-Fe-Augitic green-core Pyroxenes in the Tertiary Alkali Basalts of the Cantal Massif (French Massif Central). *Mineral. Petrol.* 76, 39–62. doi:10.1007/s007100200031

Plesner, S., Holm, P. M., and Wilson, J. R. (2002). ^{40}Ar-^{39}Ar Geochronology of Santo Antão, Cape Verde Islands. *J. Volcanol. Geotherm. Res.* 120, 103–121.

Praegel, N. O., and Holm, P. M. (2006). Lithospheric Contributions to High-MgO Basanites from the Cumbre Vieja Volcano, La Palma, Canary Islands and Evidence for Temporal Variation in Plume Influence. *J. Volcanol. Geotherm. Res.* 149, 213–239.

Price, R. C., and Chappell, B. W. (1975). Fractional Crystallisation and the Petrology of Dunedin Volcano. *Contrib. Mineral. Petrol.* 53, 157–182. doi:10.1007/bf00372602

Putirka, K. (2016). Amphibole Thermometers and Barometers for Igneous Systems and Some Implications for Eruption Mechanisms of Felsic Magmas at Arc Volcanoes. *Am. Mineral.* 101, 841–858. doi:10.2138/am-2016-5506

Putirka, K. D. (2008). 3. Thermometers and Barometers for Volcanic Systems. *Rev. Mineral. Geochem.* 69, 61–120. doi:10.1515/9781501508486-004

Putirka, K. D., Mikaelian, H., Ryerson, F., and Shaw, H. (2003). New Clinopyroxene-Liquid Thermobarometers for Mafic, Evolved, and Volatile-Bearing Lava Compositions, with Applications to Lavas from Tibet and the Snake River Plain, Idaho. *Am. Mineral.* 88, 1542–1554. doi:10.2138/am-2003-1017

Putirka, K. (1999). Clinopyroxene + liquid equilibria to 100 kbar and 2450 K. *Contrib. Mineral. Petrol.* 135, 151–163.

Putirka, K., Johnson, M., Kinzler, R., Longhi, J., and Walker, D. (1996). Thermobarometry of Mafic Igneous Rocks Based on Clinopyroxene-Liquid Equilibria, 0-30 Kbar. *Contrib. Mineral. Petrol.* 123, 92–108. doi:10.1007/s004100050145

Ranero, C. R., Torne, M., and Banda, E. (1995). Gravity and Multichannel Seismic Reflection Constraints on the Lithospheric Structure of the Canary Swell. *Mar. Geophys. Res.* 17, 519–534. doi:10.1007/bf01204342

Reagan, M. K., Turner, S., Legg, M., Sims, K. W. W., and Hards, V. L. (2008). 238U- and 232Th-decay series constraints on the timescales of crystal fractionation to produce the phonolite erupted in 2004 near Tristan da Cunha, South Atlantic Ocean. *Geochim. et Cosmochim. Acta* 72, 4367–4378. doi:10.1016/j.gca.2008.06.002

Ribeiro, O. (1954). A ilha Do Fogo e as suas erupçõēs. *Memórias, Série Geográfica I (Lisbon: Junta de Investigaçõēs do Ultramar).*

Ridolfi, F., and Renzulli, A. (2012). Calcic Amphiboles in Calc-Alkaline and Alkaline Magmas: Thermobarometric and Chemometric Empirical Equations Valid up to 1,130°C and 2.2 GPa. *Contrib. Mineral. Petrol.* 163, 877–895. doi:10.1007/s00410-011-0704-6

Ridolfi, F., Renzulli, A., and Puerini, M. (2010). Stability and Chemical Equilibrium of Amphibole in Calc-Alkaline Magmas: an Overview, New Thermobarometric Formulations and Application to Subduction-Related Volcanoes. *Contrib. Mineral. Petrol.* 160, 45–66. doi:10.1007/s00410-009-0465-7

Roedder, E. (1984). "Fluid Inclusions," in *Reviews in Mineralogy* (Mineralogical Society of America), 12, 644. doi:10.1515/9781501508271

Romero Ortiz, J. (1951). La erupción del Nambroque en la isla de La Palma. *Boletín Del. Instituto Geológico y Minero de España* 63, 3–163.

Romero Ruiz, C. (1991). *Las manifestaciones volcanicas historicas del archipielago Canario. El Cedro, S.L.: Gobierno de Canarias, Consejería de Política Territorial.*

Rout, S. S., and Wörner, G. (2020). Constraints on the Pre-eruptive Magmatic History of the Quaternary Laacher See Volcano (Germany). *Contrib. Mineral. Petrol.* 175 (8), 73. doi:10.1007/s00410-020-01710-3

Rutherford, M. J., and Hill, P. M. (1993). Magma Ascent Rates from Amphibole Breakdown; an Experimental Study Applied to the 1980-1986 Mount St. Helens Eruptions. *J. Geophys. Res.* 98 (11), 19667–19685. doi:10.1029/93jb01613

Schmidt, B. C., and Behrens, H. (2008). Water Solubility in Phonolite Melts: Influence of Melt Composition and Temperature. *Chem. Geol.* 256, 259–268. doi:10.1016/j.chemgeo.2008.06.043

Schmincke, H.-U., Klügel, A., Hansteen, T. H., Hoernle, K., and van den Bogaard, P. (1998). Bogaard, P.v.dSamples from the Jurassic Ocean Crust beneath Gran Canaria, La Palma and Lanzarote (Canary Islands). *Earth Planet. Sci. Lett.* 163, 343–360. doi:10.1016/s0012-821x(98)00168-x

Schmincke, H.-U. (1976). "The Geology of the Canary Islands," in *Biogeography and Ecology of the Canary Islands*. Editor G. Kunkel (Netherlands: The Hague), 67–184. doi:10.1007/978-94-010-1566-0_4

Shane, P., and Smith, V. C. (2013). Using Amphibole Crystals to Reconstruct Magma Storage Temperatures and Pressures for the post-caldera Collapse Volcanism at Okataina Volcano. *Lithos* 156-159, 159–170. doi:10.1016/j.lithos.2012.11.008

Shaw, C. S. J. (1999). Dissolution of Orthopyroxene in Basanitic Magma between 0.4 and 2 GPa: Further Implications for the Origin of Si-Rich Alkaline Glass Inclusions in Mantle Xenoliths. *Contrib. Mineral. Petrol.* 135, 114–132. doi:10.1007/s004100050501

Shaw, C. S. J., Thibault, Y., Edgar, A. D., and Lloyd, F. E. (1998). Mechanisms of Orthopyroxene Dissolution in Silica-Undersaturated Melts at 1 Atmosphere and Implications for the Origin of Silica-Rich Glass in Mantle Xenoliths. *Contrib. Mineral. Petrol.* 132, 354–370. doi:10.1007/s004100050429

Span, R., and Wagner, W. (1996). A New Equation of State for Carbon Dioxide Covering the Fluid Region from the Triple-Point Temperature to 1100 K at Pressures up to 800 MPa. *J. Phys. Chem. Ref. Data* 25, 1509–1596. doi:10.1063/1.555991

Sterner, S. M., and Pitzer, K. S. (1994). An Equation of State for Carbon Dioxide Valid from Zero to Extreme Pressures. *Contrib. Mineral. Petrol.* 117, 362–374. doi:10.1007/bf00307271

Sun, S.-s., and McDonough, W. F. (1989). Chemical and Isotopic Systematics of Oceanic Basalts: Implications for Mantle Composition and Processes. *Geol. Soc. Lond. Spec. Publications* 42, 313–345. doi:10.1144/gsl.sp.1989.042.01.19

Thompson, G., Smith, I., and Malpas, J. (2001). Origin of Oceanic Phonolites by crystal Fractionation and the Problem of the Daly gap: an Example from Rarotonga. *Contrib. Mineral. Petrol.* 142, 336–346. doi:10.1007/s004100100294

Torres-González, P. A., Luengo-Oroz, N., Lamolda, H., D'Alessandro, W., Albert, H., Iribarren, I., et al. (2020). Unrest Signals after 46 Years of Quiescence at Cumbre Vieja, La Palma, Canary Islands. *J. Volcanol. Geotherm. Res.* 392, 106757. doi:10.1016/j.jvolgeores.2019.106757

Turner, S., Hoernle, K., Hauff, F., Johansen, T. S., Klügel, A., Kokfelt, T., et al. (2015). ^{238}U-^{230}Th-^{226}Ra Disequilibria Constraints on the Magmatic Evolution of the Cumbre Vieja Volcanics on La Palma, Canary Islands. *J. Petrol.* 56 (10), 1999–2024. doi:10.1093/petrology/egv061

Ubide, T., Mollo, S., Zhao, J.-x., Nazzari, M., and Scarlato, P. (2019). Sector-zoned Clinopyroxene as a Recorder of Magma History, Eruption Triggers, and Ascent Rates. *Geochim. et Cosmochim. Acta* 251, 265–283. doi:10.1016/j.gca.2019.02.021

Waters, L. E., and Lange, R. A. (2015). An Updated Calibration of the Plagioclase-Liquid Hygrometer-Thermometer Applicable to Basalts through Rhyolites. *Am. Mineral.* 100, 2172–2184. doi:10.2138/am-2015-5232

Weaver, B. L. (1990). Geochemistry of highly-undersaturated ocean island basalt suites from the South Atlantic Ocean: Fernando de Noronha and Trindade islands. *Contrib. Mineral. Petrol.* 105, 502–515. doi:10.1007/bf00302491

Weis, D., Frey, F. A., Leyrit, H., and Gautier, I. (1993). Kerguelen Archipelago Revisited: Geochemical and Isotopic Study of the Southeast Province Lavas. *Earth Planet. Sci. Lett.* 118 (1), 101–119. doi:10.1016/0012-821X(93)90162-3

Weis, F. A., Skogby, H., Troll, V. R., Deegan, F. M., and Dahren, B. (2015). Magmatic Water Contents Determined through Clinopyroxene: Examples from the Western Canary Islands, Spain. *Geochem. Geophys. Geosyst* 16, 2127–2146. doi:10.1002/2015gc005800

Welsch, B., Hammer, J., Baronnet, A., Jacob, S., Hellebrand, E., and Sinton, J. (2016). Clinopyroxene in Postshield Haleakala Ankaramite: 2. Texture, Compositional Zoning and Supersaturation in the Magma. *Contrib. Mineral. Petrol.* 171 (1), 1–19. doi:10.1007/s00410-015-1213-9

Wolff, J. A., Ellis, B. S., Ramos, F. C., Starkel, W. A., Boroughs, S., Olin, P. H., et al. (2015). Remelting of Cumulates as a Process for Producing Chemical Zoning in Silicic Tuffs: A Comparison of Cool, Wet and Hot, Dry Rhyolitic Magma Systems. *Lithos* 236-237, 275–286. doi:10.1016/j.lithos.2015.09.002

Wörner, G., and Schmincke, H.-U. (1984). Petrogenesis of the Zoned Laacher See Tephra. *J. Petrol.* 25, 836–851. doi:10.1093/petrology/25.4.836

Wright, J. B. (1966). Olivine Nodules in a Phonolite of the East Otago Alkaline Province, New Zealand. *Nature* 210 (5035), 519. doi:10.1038/210519a0

Wulff-Pedersen, E., Neumann, E.-R., and Jensen, B. B. (1996). The Upper Mantle under La Palma, Canary Islands: Formation of Si–K–Na-rich Melt and its Importance as a Metasomatic Agent. *Contrib. Mineral. Petrol.* 125, 113–139. doi:10.1007/s004100050210

Wulff-Pedersen, E., Neumann, E.-R., Vannucci, R., Bottazzi, P., and Ottolini, L. (1999). Silicic Melts Produced by Reaction between Peridotite and Infiltrating Basaltic Melts: Ion Probe Data on Glasses and Minerals in Veined Xenoliths from La Palma, Canary Islands. *Contrib. Mineral. Petrol.* 137, 59–82. doi:10.1007/s004100050582

Conflict of Interest: The authors declare that the research was conducted in the absence of any commercial or financial relationships that could be construed as a potential conflict of interest.

Publisher's Note: All claims expressed in this article are solely those of the authors and do not necessarily represent those of their affiliated organizations, or those of the publisher, the editors and the reviewers. Any product that may be evaluated in this article, or claim that may be made by its manufacturer, is not guaranteed or endorsed by the publisher.